

**NASA CONTRACTOR
REPORT**



NASA CR-1467



TECH LIBRARY KAFB, NM

NASA CR-1467

LOAN COPY: RETURN TO
AFWL (WL0L-2)
KIRTLAND AFB, N MEX

**NUMERICAL CALCULATION OF
VISCIOUS COMPRESSIBLE FLUID FLOW
AROUND AN OSCILLATING RIGID CYLINDER**

by John G. Trulio and Leonard Walitt

Prepared by

APPLIED THEORY, INC.

Santa Monica, Calif.

for George C. Marshall Space Flight Center

NATIONAL AERONAUTICS AND SPACE ADMINISTRATION • WASHINGTON, D. C. • OCTOBER 1969



NUMERICAL CALCULATION OF VISCOUS COMPRESSIBLE FLUID
FLOW AROUND AN OSCILLATING RIGID CYLINDER

By John G. Trulio and Leonard Walitt

Distribution of this report is provided in the interest of information exchange. Responsibility for the contents resides in the author or organization that prepared it.

Prepared under Contract No. NAS 8-18034 by
APPLIED THEORY, INC.
Santa Monica, Calif.

for George C. Marshall Space Flight Center

NATIONAL AERONAUTICS AND SPACE ADMINISTRATION

ABSTRACT

A numerical investigation was conducted of viscous, compressible flow about a circular cylinder executing harmonic motion normal to the free stream flow direction. The oscillatory motion of the cylinder led to vortex shedding, and to a Karman vortex street. Calculations were made at a Mach number of .20, Reynolds numbers of 100 and 1000, a constant cylinder oscillation amplitude equal to 10% of the cylinder radius, and a range of cylinder oscillation frequencies. The variation with oscillation frequency of the time-averaged-drag coefficient, root-mean-squared lift coefficient, and shedding frequency, are presented. In general, increasing the cylinder oscillation frequency decreased the time-averaged drag coefficient, increased the root-mean-squared lift coefficient, and had very little effect on the shedding frequency.

TABLE OF CONTENTS

1.0	INTRODUCTION	1
1.1	Background	1
1.2	Objectives of the Program	3
1.3	Technical Approach	4
1.3.1	The Problem of a Moving Interior Boundary	4
1.3.2	Body Forces in the Frame of the Oscillating Cylinder	5
1.3.3	Boundary Flow in the Frame of the Oscillating Cylinder	6
1.3.4	Conservation in the Frame of the Oscillating Cylinder; Summary of Code Changes Due to Coordinate System Motion	6
1.4	Summary of Results	8
2.0	CALCULATIONS MADE AND RESULTS OBTAINED	10
2.1	Summary of Problems Run and Description of Mesh Used	10
2.2	Boundary Conditions Employed	11
2.3	Initial Conditions	13
2.4	Review of Numerical Results Obtained Previously for a Stationary Cylinder at a Reynolds Number of 100	14
2.5	Vortex Street Calculation for an Oscillating Cylinder at a Reynolds Number of 100	16
2.6	The Effect of Cylinder Oscillation Frequency on Vortex Shedding, Drag, and Lift	19
2.7	Effects of Reynolds Number Variation for an Oscillating Cylinder	24
3.0	CONCLUSIONS AND RECOMMENDATIONS	26
APPENDIX A	EQUATIONS OF MOTION IN A MOVING COORDINATE SYSTEM	29
APPENDIX B	AFTON 2P FINITE DIFFERENCE EQUATIONS AT INTERIOR MESH POINTS RELATIVE TO A MOVING COORDINATE SYSTEM	35
APPENDIX C	DOWNSTREAM AND LATERAL BOUNDARY CONDITIONS	41
APPENDIX D	NOMENCLATURE	46
FIGURES		49
REFERENCES		74

1.0 INTRODUCTION

1.1 Background

When launch vehicles are subjected to steady ground winds while in the vertical position, unsteady aerodynamic forces are exerted on them. These unsteady forces are associated with vortex shedding from the sides of the vehicle, and appear to be influenced by vehicle geometry, Reynolds Number, oscillatory vehicle motion, and surface conditions.

In the past, specific launch vehicle configurations have been investigated by means of dynamically scaled wind tunnel models. However, wind tunnels are limited in size. As a result, no direct tests can be made of the aerodynamic characteristics of many vehicles of interest. Instead, scaled-down models of large vehicles are examined in wind tunnels, and the resulting data are extrapolated to full vehicle size on the basis of gasdynamic scaling laws. For example, by increasing the wind speed in a wind tunnel test of a scaled-down model, the Reynolds number is raised to levels characteristic of the full-sized vehicle. For a Newtonian incompressible fluid, the two flows are then rigorously similar. However, wind speeds cannot be increased indefinitely without generating large perturbations to the flow field due to real-gas compressibility (in practice such effects are to be expected for Mach numbers greater than .3). Since large scaling factors are needed for very large vehicles such as Saturn V, it has often been necessary in wind tunnel programs to violate the scaling laws. Typically, measurements are made at lower Reynolds numbers than desired, in order to avoid drastic changes to the flow field due to compressibility at high Mach numbers. A compromise is then struck in which wind tunnel tests are conducted at lower Reynolds numbers and higher Mach numbers than would characterize the true vehicle environment according to the gasdynamic scaling laws. In the case of the Saturn V, for example, wind tunnel tests have been conducted at Reynolds numbers of about 4.5×10^6 , while the corresponding full-scale Reynolds numbers should have been about 15×10^6 .¹ Practical difficulties of scaling wind tunnel test data for large vehicles provide a strong motivation for the development of alternate procedures for determining flow fields, such as numerical integration of the equations of gasdynamic motion.

To our knowledge, there are no adequate numerical or analytical methods for calculating the complete three-dimensional flow fields about such asymmetric vehicles as the Saturn V. However, it is realistic, using existing numerical tools, to attempt to calculate flow fields about full-scale launch vehicle configurations under conditions of plane two-dimensional flow. It is also feasible in such calculations to simulate the wind-induced motion of the vehicle by forcing the body cross section to oscillate. In earlier work, vortex formation and shedding were computed around stationary body cross sections (right circular cylinders). The results were in quantitative agreement with experimental observation and with available independent theoretical calculations, to an accuracy which appeared to depend only on the length of machine time expended in computation. The numerical methods used for the computation were expected to be equally valid for flow around an oscillating body cross section.

1.2 Objectives of the Program

The primary objectives of this program were:

- a) To extend the numerical methods by which vortex flow was previously computed around stationary right circular cylinders,^{2,3} to the case in which cylinders execute harmonic motion at right angles to the free stream flow direction.
- b) To calculate flow fields about oscillating cylinders.
- c) To determine the effects of cylinder oscillation and Reynolds number on the vortex shedding frequency and on aerodynamic forces around the cylinder.

1.3 Technical Approach

The calculations of vortex shedding about stationary cylinders, noted above, were effected using a computer code called "AFTON 2P" which integrates the general equations of continuum motion subject to the assumption of plane two-dimensional symmetry. The code is based on an "explicit" finite difference representation of the equations of motion,^{3,4} by which mechanical properties at a discrete set of points (known as a "finite difference mesh"), are updated from given initial conditions to any desired later stage of motion. For this program, AFTON 2P was again applied to the special case of time-dependent viscous compressible flow.

1.3.1 The Problem of a Moving Interior Boundary

In order to extend the AFTON 2P computer code to oscillating cylinder problems, the AFTON 2P equations had to be modified to include a closed Lagrangian boundary moving inside the region of flow. The motion of a closed Lagrangian surface in the interior of an Eulerian domain presents a formidable numerical problem, to which two possible solutions were investigated.

The first method considered was based on the unique capability of the AFTON 2P code to employ arbitrary time-dependent coordinate systems. Thus, it appeared feasible to define the surface of the cylinder as one coordinate surface of a time-dependent coordinate system, with the rest of the coordinate mesh topologically identical at any instant of time to the meshes used to calculate flows around stationary cylinders. The coordinate mesh near the cylinder would then have been almost stationary with respect to the cylinder, and would have included fixed points of the cylinder's surface. At the same time, coordinate lines emanating from these surface points would terminate at the space-fixed lateral boundaries of the system. To satisfy these conditions in a simple way the mesh points would all undergo periodic motion with the same period as the cylinder, but with amplitudes decreasing smoothly to zero at the boundary of the region of calculation. However, it was concluded after some study that the boundary value problem presented by the shuttling cylinder could be handled by a second method which was as rigorous as that just outlined, but which entailed much less computer programming effort.

The procedure adopted to accommodate cylinder motion took advantage of the fact that the system contained only one moving boundary; either the Eulerian flow region boundary could be considered fixed while the cylinder boundary moved, or vice versa. By making use of a coordinate system stationary with respect to the cylinder, the entire problem of coordinate motion was reduced (apart from the addition of a simple body force) to that of calculating transport of mass, etc., across the flow region boundary; variations from the conditions of free stream flow were relatively small at that boundary. In addition, by fixing the boundary of the region of calculation with respect to the cylinder, and not with respect to an external reference frame, logical problems due to the flow of mesh points in and out of the computational domain were avoided. Thus, all points of the finite difference mesh were made to undergo the same periodic displacement with respect to a fixed external reference frame as the center of the cylinder itself; all mesh points were tied to the cylinder in rigid-body fashion. While the AFTON 2P code had to be modified somewhat to provide it with a mesh of this kind, the code changes were minimal; the required modifications are discussed in the following sections.

1.3.2 Body Forces in the Frame of the Oscillating Cylinder

In the frame of the oscillating cylinder, the cylinder's acceleration is superposed on the flow field as an apparent or "kinematic" force, and a term appears in the momentum equation to account for this force. At any instant of time the resulting kinematic acceleration, which is constant over the whole flow field, is just the negative of the acceleration of the cylinder.

The points of the cylinder were all displaced according to the equation:

$$\Delta x = A \sin \omega t \quad (1)$$

where Δx is the distance of displacement transverse to the direction of the free stream flow, and ω and A are the frequency and amplitude of oscillation of the cylinder, respectively. The code was modified to calculate the

kinematic acceleration implied by Equation 1, and that acceleration was added to the acceleration terms previously taken into account in AFTON 2P. The momentum equation in the moving coordinate system is discussed in detail in Appendices A and B.

1.3.3 Boundary Flow in the Frame of the Oscillating Cylinder

The accelerated motion of the coordinate system also led to changes in boundary conditions at the perimeter of the region of calculation. Whereas frictionless sliding had been assumed at the lateral boundaries of the system in previous calculations of flow around a stationary cylinder, the fluid now had to be given a velocity component normal to those boundaries, equal and opposite to that of the cylinder in the external reference frame. Since this component of velocity varied periodically with time, finite difference equations were formulated and programmed which describe material flow in either direction across each of the lateral boundaries. With fluid moving out of the region of calculation across a lateral boundary, that boundary became equivalent to the downstream boundary itself, and was described by downstream boundary equations developed earlier; with a minor modification for coordinate motion, exit conditions employed in this study were derived from the characteristic boundary condition used in previous stationary cylinder problems. Material entering the computational domain was simply assigned free stream properties (see Section 2.2 and Appendix C for a description of the lateral and downstream boundary condition routine employed in this program).

1.3.4 Conservation in the Frame of the Oscillating Cylinder; Summary of Code Changes Due to Coordinate System Motion

In order to preserve the mass, momentum, and energy conservation properties of the AFTON 2P equations in the moving coordinate system, two additional modifications were required. First, transport of mass, downstream momentum, and energy across lateral boundaries were included in the finite difference equations for mass, momentum, and energy conservation; previously, AFTON 2P was programmed for these effects at upstream and/or downstream boundaries. Secondly, the work of kinematic body forces had to be included

along with the surface work of boundary stresses in an equation for total energy conservation. Details of the energy conservation calculation are presented in Appendices A and B. However, the cylinder velocity superposed throughout the region of flow had no effect on the calculation of kinetic energy, since the code in its original form placed no restriction on material velocity in the interior of the calculational domain.

Thus, by viewing the flow from the frame of the cylinder, the equation and code changes necessitated by the cylinder's motion were a relatively slight generalization of the momentum and total energy calculations, and the application at lateral boundaries of conditions already provided for upstream or downstream.

1.4 Summary of Results

The principal results of the moving cylinder calculations lie in four areas.

a) The asymmetries introduced by the oscillating cylinder were sufficient to cause vortex shedding without the introduction of artificial perturbations; such perturbations were required in previous stationary cylinder problems.² As part of this program, the effects of asymmetries due to transverse cylinder motion were studied at a Reynolds number of 100, with particular reference to the shedding process. It was found that when the period of oscillation was much greater than the time, t_0 , between the start of cylinder motion and shedding, shedding first occurred on the side of the cylinder which lay in the direction of initial transverse motion. For example, when the period of oscillation was equal to $3t_0$, initial transverse motion of the cylinder in the positive x-direction (i.e., to the right with respect to the free stream) resulted in shedding of the right-hand vortex first. More generally, it was observed that regardless of the period of cylinder oscillation, vortex shedding first occurred on the side of the cylinder which accumulated the greater time-averaged shear stress in the interval t_0 .

b) On the basis of our numerical results for a Reynolds number of 100, it was found that after periodic steady-state flow was achieved, the time-averaged drag coefficient, $\overline{C_D}$, decreased slightly, and the Strouhal number, S , increased slightly, with increasing cylinder excitation frequency ϕ (see Appendix D). For instance, an increase in the dimensionless cylinder excitation frequency from 0.17 to 0.70, produced a drag coefficient decrease from 1.60 to 1.56, and a Strouhal number increase from $S = 0.17$ to $S = 0.18$.

c) Considerable root-mean-squared lift amplification took place when the dimensionless cylinder oscillation frequency, ϕ , was equal to or greater than the stationary cylinder Strouhal number, S . At a Reynolds number, R , of 100, the calculated value of S was .17, in agreement with experimental observation. With $R = 100$ and $\phi = .17$, a root-mean-squared lift coefficient of .175 was calculated; the corresponding value computed for a stationary

cylinder ($\phi = 0$) is about .134. However, for $\phi = .70$ and $R = 100$, the calculated root-mean-squared lift coefficient was 1.78 - more than ten times the corresponding stationary cylinder ($\phi = 0$) value. These results are discussed more fully in Section 2.6.

d) On the basis of numerical results at $\phi = .17$, it was found that the time-averaged drag coefficient, $\overline{C_D}$, decreased with increasing Reynolds number. With $\phi = .17$ the value of $\overline{C_D}$ was 1.60 for $R = 100$ and 0.53 at $R = 1000.0$ - a result in qualitative agreement with experimental data for stationary cylinders.

2.0 CALCULATIONS MADE AND RESULTS OBTAINED

2.1 Summary of Problems Run and Description of Mesh Used

Two stationary cylinder problems and three oscillating cylinder problems are considered in this report. The stationary cylinder problems were designated Problem 211.41 and Problem 131.0. The oscillating cylinder problems were denoted Problem 133.0, Problem 133.1, and Problem 133.2. In Problem 211.41 the formation, development, and shedding of vortices from a stationary cylinder was calculated at $R = 100.0$. Some results of Problem 211.41 were reported previously,² but lift and drag data are presented for the first time here. Problem 131.0 dealt with symmetric flow about a stationary cylinder and was run primarily to generate initial data for the moving cylinder problems. In Problems 133.0 and 133.2 the cylinder oscillation frequency was varied at $R = 100.0$. The Reynolds number was 1000.0 in Problem 133.1, while the cylinder oscillation frequency was the same as that of Problem 133.0. In each problem the cylinder radius was 1.5 cm, the free stream Mach number was 0.20, and the amplitude of oscillation of the cylinder was equal to a tenth of its radius. A summary of parameter values for the problems of the program is presented in Table 1.

The finite difference mesh which was used in all moving cylinder problems and in the stationary cylinder problem 131.0, consisted of 3520 points and is shown in Figure 1. The upstream boundary is located 6.6 diameters from the cylinder center, where it has little effect on the flow field in the neighborhood of the cylinder. The mesh was also used for Problem 211.41, except that the upstream boundary was located 2.25 diameters from the cylinder center.

2.2 Boundary Conditions Employed

In all calculations the density, specific internal energy, and velocity of material in the y-direction (the free stream direction; see Figure 1), were given their free stream values at the upstream boundary. For the stationary cylinder problems, the velocity of material in the x-direction was zero at the upstream boundary. However, since the moving cylinder problems of the program employed a mesh which was stationary in the frame of the cylinder (see Section 1.3), the x-component of material velocity at the upstream boundary was set equal and opposite to the cylinder velocity in the laboratory frame.

As noted in Section 1.3.4, the method used to compute downstream boundary flow for all problems of this program was developed for previous stationary cylinder calculations,^{2,3} and is based on the method of characteristics. The generalization to the case of interest here, in which the boundary moves with respect to the lab frame, is given in Appendix C.

In the stationary cylinder problems, fluid was allowed to slide without friction along the lateral boundaries, i.e., at a lateral boundary the normal component of material velocity, and the tangential stress, were zero. For the moving cylinder problems, which were solved numerically in a frame stationary with respect to the cylinder (Section 1.3), mass, etc., flowed across the lateral boundaries of the finite difference mesh either from the free stream to the mesh, or from the mesh to the free stream. When the lateral boundary moved into the free stream, transport took place from the free stream to the mesh, and free stream conditions were imposed at the boundary. On the other hand, when the lateral boundary moved away from the free stream, then the characteristic boundary condition (Section 1.3.2) was used if mass flowed across the boundary out of the mesh, and free stream conditions were used if mass flowed into the mesh (see Appendix B for details of the characteristic boundary condition). These rules led to stable numerical flow fields near the lateral boundaries of the oscillating cylinder problems (see Section 2.5 for further discussion).

Finally, a no-slip boundary condition was imposed at the cylindrical surface in all problems. For the stationary cylinders, the velocity of fluid at the cylinder surface was then set equal to zero. For the moving cylinder problems, the surface velocity was zero in the computational frame, which was fixed with respect to the cylinder.

2.3 Initial Conditions

Apart from the no-slip condition imposed at the cylinder surface, the two stationary cylinder problems (Problems 211.41 and 131.0) were started from impulsive initial conditions, i.e., conditions of uniform velocity, density, and energy. The flow field about a full stationary cylinder at a Reynolds number of 100.0 (Problem 131.00; see Table 1), and at a characteristic time τ of 2.7, was subsequently taken as the initial field of flow for the moving cylinder problems. At $\tau = 2.7$, a symmetrical vortex pair had developed in Problem 131.00, with a rear stagnation point located about 3.2 cylinder radii downstream of the cylinder center; the vortex centers were located about 1.855 cylinder radii from the cylinder center. The flow field for Problem 131.00 at a characteristic time of 2.7 is shown in the form of a velocity vector plot in Figure 2. The vectors of Figure 2 are proportional to the particle velocities at the points of the finite difference mesh; a mesh point is located at the tail of each vector.

2.4 Review of Numerical Results Obtained Previously for a Stationary Cylinder at a Reynolds Number of 100

Vortex formation, development, and shedding were calculated about a stationary cylinder at a free stream Reynolds number of 100, and at a free stream Mach number of .20 (Problem 211.41; see Table 1). This system, which was otherwise symmetric about a plane through the cylinder axis, was perturbed asymmetrically to induce vortex shedding. The calculation was then carried through the shedding of five vortices. When a periodic state had been reached, the computed flow field contained a vortex sheet with a shedding frequency within 10% of the value measured for $R = 100.0$, namely, $S = .17$.

The time-averaged drag coefficient, time-averaged lift coefficient, and root-mean-squared lift coefficient were also found from the stress field of Problem 211.41. For this purpose, the instantaneous force of the fluid on the cylinder was computed by integrating numerically the stress component normal to cylinder surface and the stress component tangential to the cylinder surface, over the cylinder surface. The component of the resultant force along the direction of free stream flow defines the drag force, and the component normal to the free stream flow direction is the lift force. The instantaneous lift and drag coefficients were then determined from the relations

$$C_D = \frac{\text{Drag Force}}{\frac{1}{2}\rho_\infty U_\infty^2 D} \quad (2)$$

$$C_L = \frac{\text{Lift Force}}{\frac{1}{2}\rho_\infty U_\infty^2 D} \quad (3)$$

where ρ_∞ is the free stream density, U_∞ is the free stream velocity, and D is the cylinder diameter. Finally, time-averaged lift and drag coefficients were found by numerical evaluation of the following integrals

$$\bar{C}_D = \frac{1}{t} \int_0^t C_D dt' \quad (4)$$

$$\bar{C}_L = \frac{1}{t} \int_0^t C_L dt' \quad (5)$$

where the time t is measured from the start of cylinder motion. The root-mean-squared lift coefficient was determined by numerical evaluation of the integral

$$C_L(\text{r.m.s.}) = \left[\frac{1}{t} \int_0^t C_L^2 dt' \right]^{\frac{1}{2}} \quad (6)$$

For Problem 211.41, the time-averaged drag coefficient approached the value $\bar{C}_D = 1.7$, which is approximately 3% lower than the value of C_D measured by C. Wieselsberger⁶. The time-averaged lift coefficient was zero; the instantaneous lift coefficient oscillates about zero in a periodic manner. However, the calculated root-mean-square lift coefficient, $C_L(\text{r.m.s.})$, was .134.

2.5 Vortex Street Calculation for an Oscillating Cylinder at a Reynolds Number of 100

In the first moving cylinder problem attempted (Problem 133.0; see Table 1) the flow field was calculated about a right circular cylinder at a Reynolds number of 100.0. The cylinder was made to oscillate at a frequency corresponding to a Strouhal number of .17. As previously noted, the initial state of motion for Problem 133.0 was specified as the flow field of Problem 131.0 at a characteristic time of 2.7; the cylinder displacement was prescribed by Equation (1), and the double amplitude of oscillation was 10% of the cylinder diameter. Problem 133.0 was run to a characteristic time of 10.9, which corresponds to about 1.5 cycles of cylinder oscillation. As can be seen from Equation (1), the cylinder moved initially in the positive x-direction (to the right), and shedding began with the right-hand vortex at a characteristic time of approximately 4.63 (about .85 msec after the start of the cylinder oscillation). When shedding took place, ($\tau = 4.63$), the cylinder had completed about a third of its cycle of motion, with a time-averaged displacement, $\bar{\Delta x}$, of .1085 cm in the positive x-direction.

That vortex shedding took place first on the right side of the cylinder is consistent with the fact that the shear stress was larger on the right than on the left, in the period prior to shedding. A larger shear stress on the right than on the left is a physically reasonable outcome of the cylinder's initial left-to-right transverse motion; the right boundary layer is compressed while the left layer expands, and the normal gradient of tangential velocity should therefore be larger on the right than on the left. It can be seen from Figure 3 that the numerical results bear out these observations; time histories of shear stress on the right- and left-hand cylindrical surface are presented in Figure 3, at points plus and minus ninety degrees from the forward stagnation point of the cylinder (i.e., at the points $x = 1.5$ cm, $y = 0.0$ cm, and $x = -1.5$ cm, $y = 0.0$ cm respectively). The time scale in Figure 3 is measured from the start of cylinder oscillation, when $t = 1.19$ msec and $\tau = 2.7$. From Figure 3 it is seen that the shear stress is greater on the right than on the left up to a time of .85 msec, or $\tau \approx 4.1$.

Vortex shedding in Problem 133.0 is illustrated by Figures 4 - 7, in the form of velocity vector plots. In Figure 4 (at a characteristic time of 7.08), the first right-hand vortex has moved far downstream, and the first left-hand vortex is also seen to be moving downstream. The displacement of the cylinder at $\tau = 7.08$ is also exhibited in Figure 4, since the cylinder's center was initially coincident with the indicated space-fixed origin of coordinates; velocity vectors and mesh points are all shown relative to the space-fixed frame. At a characteristic time of 7.95 (Figure 5), the first left-hand vortex is still propagating downstream, and a second right-hand vortex has begun to form. In Figure 6 ($\tau = 8.9$), the first left-hand vortex has moved still farther downstream, while the second right-hand vortex has become fully formed. The velocity vector plot of Figure 7 ($\tau = 10.45$) shows the second right-hand vortex shedding, and another left-hand vortex forming. As can be seen from Figures 4 - 7, the flow at the lateral boundaries is essentially free stream flow, with no evidence of numerical instabilities; the lateral boundary condition imposed in Problem 133.0 therefore appears satisfactory for flows of this type.

After many vortices have shed, the flow is experimentally observed to be almost periodic; a vortex detaches itself first from one side of the cylinder, then from the other side, and so on. Under conditions of near-periodic flow, times of arrival of successive vortex centers along a given line normal to the center line of the system, are almost equally spaced.

In order to obtain a periodic flow field, Problem 133.0 was run far enough to permit the shedding of four vortices. From a careful examination of velocity vector plots, the trajectories of the centers of the four vortices were determined. These trajectories are shown in Figure 8, where y/a is plotted as a function of time ("y" is the streamwise position coordinate and "a" the cylinder radius). The time between the passage of Left Hand Vortex One (LHV1) and Right Hand Vortex Two (RHV2) at $y/a = 3.9$ was 1.26 msec, and the time period

between the passage of RHV2 and LHV2 at $y/a = 1.6$, was 1.28 msec (see Figure 8; shedding began on the right). Since these time periods are within 2% of each other, it is assumed that near-periodic flow exists 2.32 msec after the start of cylinder oscillation. By doubling the time differences cited, numerical approximations to the vortex shedding period were obtained; expressed as dimensionless Strouhal numbers (Appendix D) the period found at $y/a = 3.9$ was .175 and at $y/a = 1.6$ the period was .172. The measured Strouhal number for a stationary cylinder at $R = 100.0$ is .17.

Based on Equations (2) through (6), values of the coefficients of time-averaged drag, time-averaged lift, and root-mean squared lift were computed for Problem 133.0. The time-averaged drag coefficient was 1.60 - about 6% less than that calculated for a stationary cylinder at a Reynolds number of 100.0 (see Section 2.4). The time-averaged lift coefficient was zero. The root-mean squared lift coefficient was .175, a value approximately 30% greater than the root-mean-squared lift coefficient calculated for a stationary cylinder at a Reynolds number of 100.0 (Problem 211.41; see Section 2.4). The lift amplification calculated for a cylinder oscillation frequency equal to the stationary cylinder shedding frequency, is consistent with available experimental results. Cincotta¹ experimentally investigated unsteady aerodynamic lift forces on oscillating cylinders over a range of Reynolds numbers from $.4 \times 10^6$ to 10.7×10^6 . Root-mean-squared lift amplification was observed when the model oscillation frequency was approximately equal to the stationary model shedding frequency.

2.6 The Effect of Cylinder Oscillation Frequency on Vortex Shedding, Drag, and Lift

To determine the effect of the cylinder oscillation frequency on the shedding frequency, time-averaged drag coefficient, and root-mean-squared lift coefficient, the frequency of oscillation of the cylinder was increased to an equivalent Strouhal number value of .70 (Problem 133.2, see Table 1). Initial conditions were again those of the flow field of Problem 131.0 at a characteristic time of 2.7 (see Section 2.3), and the Reynolds number was 100.0. For Problem 133.2 vortex shedding is illustrated in the velocity vector plots of Figure 9 - 12; at the increased cylinder oscillation frequency of Problem 133.2, the velocities of the mesh points on the cylindrical surface are large enough to appear in the vector plots.

Although the cylinder moved initially in the positive x-direction (to the right, as in Problem 133.0), the left-hand vortex shed first in Problem 133.2, at a characteristic time τ of 5.30. In the velocity vector plot of Figure 9 ($\tau = 7.17$), the left-hand vortex is displaced slightly downstream of the right-hand vortex. Shedding of the left-hand vortex first, despite the initial left-to-right cylinder motion, is consistent with the fact that the time-averaged shear stress was greater on the left than on the right at the time shedding took place. The possibility of such shear stress history arises when the transverse oscillation frequency exceeds the vortex shedding frequency. Other things being equal, if vortex growth is slight over a period of transverse oscillation, then circulation will accumulate on the left and right in about equal amounts in one cycle. Since the cylinder starts from its mean position, right to left motion begins after a quarter of a cycle is complete; circulation on the left will then tend to exceed that on the right during the third quarter-cycle, and any shedding in that interval would take place on the left. Actually, the initial incidence of shedding is complicated by vortex growth, and by other transients arising from both the initial conditions of flow and cylinder motion; circulation does not accumulate on the right during the first and fourth quarters of a cycle, in just the same way as on the left during the second and third quarters. As a result, to give a convincing account of initial shedding on the left may require a detailed understanding of relatively minor aspects of the motion, particularly if the oscillation frequency is much greater than the shedding frequency. In Problem 133.2 the frequency of oscillation was about twice that for shedding.

Figure 13 shows shear stress histories for Problem 133.2 at points on the right- and left-hand cylindrical surfaces; the points are located ninety degrees (plus and minus) from the forward stagnation point of the cylinder (see Figure 1). The time axis of Figure 13 is measured with respect to the start of cylinder oscillation. Based on the results presented in Figure 13, time-averaged shear stresses $\bar{\tau}_{xy}(\ell)$ and $\bar{\tau}_{xy}(r)$ were determined on the left and right sides of the cylinder, respectively, by numerical evaluation of the following integrals:

$$\bar{\tau}_{xy}(\ell) = \frac{1}{t} \int_0^t \tau_{xy}(\ell) dt' \quad (7)$$

$$\bar{\tau}_{xy}(r) = \frac{1}{t} \int_0^t \tau_{xy}(r) dt' \quad (8)$$

where $\tau_{xy}(\ell)$ and $\tau_{xy}(r)$ are instantaneous shear stresses at the left- and right-hand points, and t is the time. Shedding occurred 1.146 msec after the start of cylinder motion (i.e., at a characteristic time τ equal to 5.30), when the time-averaged shear stresses on the right and left, respectively, were $\bar{\tau}_{xy}(r) = .00420$ and $\bar{\tau}_{xy}(\ell) = .00455$. In Problem 133.0 (see Figure 3) the instantaneous shear stress was always greater on the right prior to shedding, and the right hand vortex shed first (see Section 2.4). Thus, the results of Problems 133.0 and 133.2 are consistent with the idea that vortex shedding will occur on the side of the cylinder having the greater time-averaged shear stress at the time of shedding.

Based on Equations (2) - (5), time-averaged lift and drag coefficients were computed for Problem 133.2. The time-averaged lift coefficient was zero, i.e., the instantaneous lift coefficient oscillates about zero. The time-averaged drag coefficient was 1.56 - about 11% less than that of a stationary cylinder at a Reynolds number of 100.0. The time-averaged drag coefficient is shown in Figure 14 as a function of cylinder oscillation frequency.

It can be seen from Figure 14 that the drag decreases with increasing oscillation frequency, a dependence that appears qualitatively correct. Due to the transverse velocity of the cylinder, which is directly proportional to the amplitude, A , and frequency of oscillation, ω ; (see Equation (1)), the instantaneous speed of free stream flow relative to the cylindrical surface will be equal to or greater than the free stream speed relative to a laboratory frame. Thus, the instantaneous Reynolds number, R' , relative to the cylinder, and based on the cylinder's diameter, will always be greater than or equal to the Reynolds number, R , relative to the laboratory frame. Therefore, if the time-averaged Reynolds number, \bar{R}' , relative to the moving cylinder is defined as

$$\bar{R}' = \frac{1}{2\pi} \int_0^{2\pi} R' d\theta \quad (9)$$

where $\theta = \omega t$, then $\bar{R}' \geq R$. Experimentally it has been found that the drag coefficient for a stationary cylinder varies inversely with Reynolds number⁶. Therefore, the numerical result that at constant oscillation amplitude the drag coefficient decreases with increasing cylinder oscillation frequency appears at least qualitatively correct.

The increase in the Reynolds number, \bar{R}' , with the cylinder oscillation frequency, ω , can be used to establish a qualitative relation between ω and the time-averaged boundary layer thickness, $\bar{\delta}$, on the cylindrical surface. Since \bar{R}' increases with ω , the local Reynolds number per unit length around a cylindrical cross-section also increases as ω increases. Recalling that the boundary layer thickness, is inversely proportional to the square root of the local Reynolds number, it follows that $\bar{\delta}$ should decrease with increasing cylinder oscillation frequency. For an infinite flat plate executing simple harmonic motion with frequency ω along the direction of free stream flow⁸, the effective boundary layer at the plate has the thickness

$$\bar{\delta} \sim \sqrt{\frac{\nu}{\omega}} \quad (10)$$

where ν is the kinematic viscosity; similar results apply for other solid surfaces oscillating in a fluid at rest or for a fixed surface in an oscillating stream⁹. Thus, the decrease in boundary layer thickness with oscillation frequency, found in the results of Problems 133.0 and 133.2, is not only physically understandable, but also has a firm theoretical basis in unsteady boundary layer theory.

After a periodic steady-state was achieved, the vortices in Problem 133.2 shed at a Strouhal number of .18. The variation of Strouhal number with cylinder oscillation frequency, for a constant double amplitude of oscillation equal to 10% of the cylinder diameter, is shown in Figure 15. As can be seen from Figure 15, increasing the cylinder oscillation frequency causes a slight increase in shedding frequency, as one might expect; the effective Reynolds number \bar{R} increases with frequency, and the Strouhal number is known experimentally to increase with Reynolds number.

To establish a relation between transverse cylinder motion and the direction of the instantaneous lift force on the cylinder, the instantaneous lift coefficient was studied as a function of time for Problem 133.2 after a periodic state had been achieved. The time variation of the instantaneous lift coefficient, cylinder displacement, and cylinder acceleration are shown in Figure 16. A positive lift coefficient indicates a force in the positive x-direction (see Figure 1). Aside from a small phase angle, it can be seen from Figure 16 that the aerodynamic lift force on the cylinder generally opposes the cylinder acceleration, a result believed to hold for any cylinder oscillation frequency.

From the instantaneous coefficients of Figure 16 and Equations (3) and (6), a root-mean-squared lift coefficient of 1.78 was computed for a cylinder oscillation frequency corresponding to a Strouhal number of 0.70 (Problem 133.2). The root-mean-squared lift is therefore about ten times larger for a cylinder oscillation frequency corresponding to a Strouhal number of 0.70 (Problem 133.2),

than for an equivalent Strouhal number of 0.17 (Problem 133.0)--a tremendous lift increase. The rapid growth of lift with oscillation frequency reflects a corresponding growth in the transverse pressure difference across the cylinder, as the oscillation frequency increases. The pressure distribution on the cylindrical surface, at a cylinder oscillation frequency corresponding to $\phi = 0.17$ (Problem 133.0), and at a time when a periodic motion was achieved ($\tau = 10.45$; see Figure 7), is presented in Figure 17. In Figure 17 the pressure is greater on the right-hand cylindrical surface than on the left-hand surface, and the lift force is therefore in the positive x-direction. The area between the curves defines the pressure force contribution to the lift and corresponds to a positive pressure lift coefficient, C_{LP} , equal to 0.127, a value approximately 24 percent less than the total instantaneous lift. The pressure distribution on the cylindrical surface at a cylinder oscillation frequency corresponding to $\phi = 0.70$ (Problem 133.2), and at a characteristic time τ of 10.05, is shown in Figure 18. A velocity vector plot of the flow field at this time is presented in Figure 12. In this case the pressure is generally higher on the right-hand surface than on the left, and the lift force is in the negative x-direction. The area between the right- and left-hand curves now corresponds to $C_{LP} = -0.804$, a value which is about 23 percent smaller than the total instantaneous lift, but about 6.3 times that cited above for Problem 133.0. Such a result is qualitatively reasonable; as the cylinder oscillation frequency increases, the maximum compression of fluid increases on the side of the cylinder in the direction of motion, while the minimum compression decreases on the other side. Lift forces should therefore grow with cylinder oscillation frequency, as the numerical results indicate.

The variation of the root-mean-squared lift coefficient, C_L (r.m.s.), with cylinder oscillation frequency is presented in Figure 19. The curve faired through the data is based on the experimental results of Cincotta¹, which show a peak value of C_L (r.m.s.) at the aerodynamic shedding frequency for a stationary cylinder ($S = 0.17$); C_L (r.m.s.) then decreases with S reaching the stationary cylinder root-mean-squared lift coefficient at approximately twice the aerodynamic Strouhal number for a stationary cylinder. Cincotta's data are also shown in the figure.

2.7 Effects of Reynolds Number Variation For an Oscillating Cylinder

To investigate the influence of Reynolds number on the shedding frequency, drag, and root-mean-squared lift, the flow field about an oscillating cylinder was calculated at a Reynolds number of 1000.0 (Problem 133.1). The cylinder oscillation frequency and amplitude were the same as those of Problem 133.0. The finite difference mesh consisted of the two-dimensional array of 44 x 80 points shown in Figure 1. The initial flow field was again identical to that of Problem 131.0 at a characteristic time of 2.7, when a symmetrical vortex pair had already developed. The sudden increase in Reynolds number caused apparently random oscillations in the pressure on the cylindrical surface, and subsequently in the instantaneous drag coefficients. After approximately 250 timesteps of calculation these oscillations appeared to have damped out, and the flow was assumed to be that appropriate to a Reynolds number of 1000.0. The calculation was continued for 1.5 shedding periods.

Vortex shedding in Problem 133.1 is illustrated by the velocity vector plots of Figures 20 - 23. As in the case of Problem 133.0, the right-hand vortex shed first, but now at a characteristic time τ of 4.63. Initial shedding on the right was due to initial transverse motion of the cylinder in the positive x-direction with a period much longer than the time needed to induce shedding (see Section 2.6). A comparison of the wake at a Reynolds number of 1000.0 (Figure 23, $\tau = 9.08$) with that at a Reynolds number of 100.0 (Figure 7, $\tau = 10.45$), indicates a more random set of velocity vectors for $R = 1000.0$. The turbulent character of the wake at $R = 1000.0$ is consistent with our previous results regarding pressure oscillations recorded on the leeward side of a cylinder³, and with the experimental results of Roshko⁵. Earlier numerical calculations resulted in pressure variations which were smooth at $R = 100.0$, but exhibited elements of randomness at $R = 1000.0$; Roshko found that the vortex street from a cylinder was laminar at a Reynolds number of 100, and turbulent at a Reynolds number of 1000.0.

Based on the numerical results of Problem 133.1, the effects of Reynolds number on the shedding frequency, drag, and lift were determined. When a periodic steady state had been achieved, the vortices shed at a Strouhal number of 0.21, which corresponds to the Strouhal number measured for a stationary cylinder at $R = 1000.0$. The time-averaged drag coefficient was 0.53. A drag coefficient of 0.53 is approximately half that of a stationary cylinder at $R = 1000.0$; this result is consistent with the drag dependence found at $R = 100$ as the cylinder oscillation frequency increased. The time-averaged drag coefficient is presented in Figure 24 as a function of Reynolds number for a cylinder oscillation frequency corresponding to a Strouhal number of 0.17. The stationary cylinder data presented in Figure 24 were used as a basis for fairing the curve shown for the oscillating cylinder. It can be seen from Figure 24 that, as in the case of a stationary cylinder, the drag coefficient decreases with Reynolds number. In the oscillatory case, the computed root-mean-squared lift coefficient was about 0.18; the calculation for a stationary cylinder at $R = 1000.0$ was part of an earlier program in which C_L (r.m.s.) was not computed, nor to our knowledge have root-mean-squared lift data been measured.

3.0 CONCLUSIONS AND RECOMMENDATIONS

The work summarized in this report constitutes our first attempt to extend the AFTON 2P code, and the numerical methods it embodies, to problems of viscous, compressible flow about accelerating structures. The principal conclusion reached in the work reported here is similar to that of our stationary cylinder calculations³: up to a Reynolds number of 5000 complete flow fields about accelerating bodies can, at feasible cost, be predicted quantitatively by AFTON 2P with an accuracy sufficient for almost any practical purpose. Furthermore, by incorporating a variable timestep into the numerical technique, it is quite likely that an accuracy comparable to that obtained in the problems reported here can be achieved up to a Reynolds number of 15×10^6 (the Reynolds number for a full scale Saturn V vehicle) and for a class of two-dimensional accelerating bodies which includes most shapes of practical interest.

These conclusions rest both on numerical results obtained previously for stationary cylinders^{2,3}, and on the specific results discussed in detail in Section 2.0. The basic supporting facts will now be summarized.

Our previous stationary cylinder calculations were performed in two separate programs. In the first program, it was established that for right cylinders of fairly simple shape, important gross parameters such as lift, drag, and Strouhal number could be calculated up to Reynolds numbers of 1000.0. For example, at a Reynolds number of 100, the calculated drag coefficient was within 3% of the experimental value and Strouhal number was within 10% of the measured value (see section 2.4). However, no significant effort was devoted to determining the accuracy of the numerical predictions for the pressure and velocity fields. In the second program, detailed calculations were performed at Reynolds numbers of 100 and 1000, with finite difference

meshes that were much finer than any used in the first program. The AFTON boundary layer profiles along normals to the cylinder were nowhere in error by as much as 1%, as determined by comparison with the known exact solution. The pressure coefficient distribution around the cylinder at a stage of substantial vortex development, for a Reynolds number of 100 and a Mach number of .2, was within 15% of an independent incompressible viscous flow calculation; the AFTON 2P fluid is compressible. Furthermore, a study of the numerical solution error showed that the mesh point density could be made sufficiently large in practice to reduce the maximum pressure coefficient error for the entire cylindrical surface to no more than 1.4%. Thus by employment of finer meshes, any desired solution accuracy can be obtained.

In the oscillating cylinder problems presented in Section 2.0, vortex shedding was initiated by the asymmetries introduced by the shuttling cylinder, without the introduction of artificial perturbations. This result conforms to experimental observation. The finite difference mesh employed in these oscillating cylinder problems was identical to that employed in the stationary cylinder problems of our first program. Thus, it is reasonable to assume that the accuracy of the calculated lift, drag, and Strouhal number in the oscillating cylinder problems is appropriate to the corresponding stationary cylinder parameters calculated in the first program. Furthermore, the calculated relationships between the cylinder oscillation frequency and the root-mean-squared lift coefficient, time-averaged drag coefficient and Strouhal number are qualitatively consistent with clear and simple physical considerations (see Section 2.6). Finally, since increased accuracy was achieved at feasible cost by mesh refinement in the stationary cylinder problems of our second program, it appears that a similar increase in accuracy can be attained by employing finer meshes in the moving cylinder problems.

A development important to future calculations lies in the discovery of finite difference equations which preserve all the properties of self-consistency of the present equations, but in which the time-step can be varied from zone to zone. In this way, the variables of motion need only be calculated for a given zone as often as required by considerations of stability for that zone and its immediate neighbors, rather than for the least stable zone of the finite difference mesh. The increase in speed of solution of problems like those reported here was potentially so great that variable timestep (VTS) equations were investigated in one space dimension. An increased speed of solution by a factor of five was obtained. This factor should be even greater in two dimensions, using a two-dimensional counterpart of our one-dimensional VTS scheme. It is therefore recommended that a variable timestep be incorporated into the AFTON 2P computer code for moving cylinders, and that a numerical investigation be conducted of flow fields about oscillating cylinders in the higher Reynolds number regime (i.e., 10^6 to 15×10^6). The experimental data of J.J. Cincotta could be used to establish the accuracy of the numerical results in this range of Reynolds number.

APPENDIX A

EQUATIONS OF MOTION IN A MOVING COORDINATE SYSTEM

In this section the integral equations of motion are developed in a coordinate system fixed relative to a moving obstacle immersed in a viscous, compressible fluid.

The integral equations of motion in the moving coordinate system will be derived in Cartesian tensor notation¹⁰, where the position vector is defined by x_i and the velocity vector is defined by u_i ($i = 1, 2, \text{ or } 3$). Consider a volume τ of three-dimensional space having a surface area Γ which is a fixed relative to a laboratory frame. In partial differential form, the conservation equations are as follows relative to the laboratory frame:

Continuity

$$\frac{\partial \rho}{\partial t} + \frac{\partial}{\partial x_\beta} (\rho u_\beta) = 0 \quad (11)$$

where t is the time, ρ is the density, and, by the summation convention, the repeated indices indicate the summation

$$\frac{\partial}{\partial x_\beta} (\rho u_\beta) = \frac{\partial}{\partial x_1} (\rho u_1) + \frac{\partial}{\partial x_2} (\rho u_2) + \frac{\partial}{\partial x_3} (\rho u_3)$$

First Law

$$\frac{\partial (\rho E)}{\partial t} + \frac{\partial (\rho u_\beta E)}{\partial x_\beta} = P_{\beta\alpha} \frac{\partial u_\alpha}{\partial x_\beta} \quad (12)$$

where E is the specific internal energy and $P_{\beta\alpha}$ is the stress tensor.

Momentum

$$\frac{\partial(\rho u_\alpha)}{\partial t} + \frac{\partial}{\partial x_\beta} (\rho u_\beta u_\alpha) = \frac{\partial P_{\beta\alpha}}{\partial x_\beta} \quad (13)$$

The transformation equations relating the laboratory and moving frames will now be presented. Consider a moving coordinate system with a position vector x_i and velocity vector u_i measured relative to this system. Let the velocity of the moving coordinate system be denoted $V_i(t)$ ($i = 1, 2, \text{ or } 3$). The relationship between the laboratory frame and the moving frame can be defined by the following Galilean transformation:

$$\left. \begin{aligned} x_i &= x'_i + \int V_i(t) dt \\ t &= t' \end{aligned} \right\} \quad (14)$$

where t' is the time in the moving frame. Based on the transformation equations (14) the partial derivatives in the laboratory and moving frames may be related as follows:

$$\left. \begin{aligned} \frac{\partial}{\partial x_i} &= \frac{\partial}{\partial x'_i} \\ \frac{\partial}{\partial t} &= \frac{\partial}{\partial t'} - V_i \frac{\partial}{\partial x'_i} \end{aligned} \right\} \quad (15)$$

Finally the particle velocities in the laboratory and moving frames are related as follows:

$$u_i = u'_i + V_i(t) \quad (16)$$

Based on the above transformation equations, the conservation laws relative to the laboratory frame Equations (11), (12) and (13), can be transformed to the moving frame. The conservation equations relative to the moving frame are as follows:

Continuity

$$\frac{\partial \rho}{\partial t'} + \frac{\partial}{\partial x'_\beta} (\rho u'_\beta) = 0 \quad (17)$$

First Law

$$\frac{\partial (\rho E)}{\partial t'} + \frac{\partial}{\partial x'_\beta} (\rho E u'_\beta) = P_{\beta\alpha} \frac{\partial u'_\alpha}{\partial x'_\beta} \quad (18)$$

where the stress tensor $P_{\beta\alpha}$ remains unchanged since it is proportional to $\frac{\partial u_\alpha}{\partial x_\beta}$ which is unaffected by the transformation.

Momentum

$$\frac{\partial \rho u'_\alpha}{\partial t'} + \frac{\partial}{\partial x'_\beta} (\rho u'_\beta u'_\alpha) + \rho \frac{dV_\alpha}{dt} = \frac{\partial P_{\beta\alpha}}{\partial x'_\beta} \quad (19)$$

It is seen from the transformed Equations (17), (18) and (19) that, as discussed in Section 1.3, only the momentum equation has changed in the moving coordinate system. From the Gauss Theorem, relating a volume integral to a surface integral, Equations (17), (18) and (19) can be transformed to integral form. The Gauss Theorem is as follows:

$$\int_{\Gamma'} g'_\beta d\Gamma' = \int_{\tau'} \frac{\partial g}{\partial x_\beta} d\tau' \quad (20)$$

where τ' is the fixed volume τ defined relative to the moving coordinate surface ($\tau' = \tau$), Γ' is the surface area of Γ defined relative to the moving coordinate system ($\Gamma' = \Gamma$), g is any tensor defined within τ' and whose derivatives are continuous there, and l'_β is the direction cosine of the normal to the surface Γ' in the direction β . Based on Equation (20) the final integral equations of motion relative to moving coordinate system become:

Continuity

$$\frac{\partial}{\partial t'} \int_{\tau'} \rho d\tau' = \int_{\Gamma'} \rho u'_\beta l'_\beta d\Gamma' \quad (21)$$

First Law

$$\frac{\partial}{\partial t'} \int_{\tau'} \rho E d\tau' + \int_{\Gamma'} \rho u'_\beta E l'_\beta d\Gamma' = \int_{\tau'} P_{\beta\alpha} \frac{\partial u'_\alpha}{\partial x'_\beta} d\tau' \quad (22)$$

Momentum

$$\begin{aligned} & \frac{\partial}{\partial t'} \int_{\tau'} \rho u'_\alpha d\tau' + \int_{\Gamma'} \rho u'_\beta l'_\beta u'_\alpha d\Gamma' \\ & + \left(\int_{\tau'} \rho d\tau' \right) \frac{dv'_\alpha}{dt'} = \int_{\Gamma'} P_{\beta\alpha} l'_\beta d\Gamma' \end{aligned} \quad (23)$$

The body force term $\left(\int_{\tau'} \rho d\tau' \right) \frac{dv'_\alpha}{dt'}$ in Equation (23) is the only term which must be added to the equations of motion to make them valid in the moving frame.

In order to preserve the energy conservation property of the AFTON 2P equations in the moving coordinate system, a kinematic work

term must be subtracted from the surface work term in the total energy conservation equation. The total energy conservation equation in the moving frame can be derived from the Momentum equation (Equation 19) and First Law Equation (20). First the kinetic energy equation in the moving frame is derived by multiplying Equation (19) by u'_α , i.e.,

Kinetic Energy Equation

$$\frac{\partial}{\partial t'} \left(\rho \frac{u'_\alpha u'_\alpha}{2} \right) + \frac{\partial}{\partial x'_\beta} \left(\rho u'_\beta \frac{u'_\alpha u'_\alpha}{2} \right) + \rho u'_\alpha \frac{dv_\alpha}{dt} = u'_\alpha \frac{\partial P_{\beta\alpha}}{\partial x'_\beta} \quad (24)$$

Adding Equations (18) and (24) yields the total energy equation in partial differential form

$$\begin{aligned} \frac{\partial}{\partial t'} \left[\rho \left(E + \frac{u'_\alpha u'_\alpha}{2} \right) \right] + \frac{\partial}{\partial x'_\beta} \left[\rho u'_\beta \left(E + \frac{u'_\alpha u'_\alpha}{2} \right) \right] \\ + \rho u'_\alpha \frac{dv_\alpha}{dt'} = \frac{\partial}{\partial x'_\beta} (P_{\beta\alpha} u'_\alpha) \end{aligned} \quad (25)$$

By utilizing the Gauss Theorem, Equation (20), Equation (25) can be put into the integral form

$$\begin{aligned} \frac{\partial}{\partial t'} \int_{\tau'} \rho \left(E + \frac{u'_\alpha u'_\alpha}{2} \right) d\tau' + \int_{\Gamma'} \rho u'_\beta \left(E + \frac{u'_\alpha u'_\alpha}{2} \right) l'_\beta d\Gamma' \\ = \int_{\Gamma'} P_{\alpha\beta} u'_\alpha d\Gamma - \left(\int_{\tau'} \rho u'_\alpha d\tau' \right) \frac{dv_\alpha}{dt} \end{aligned} \quad (26)$$

where it can be shown that $P_\alpha d\Gamma' = P_{\beta\alpha} l_\beta' d\Gamma'$. Equation (26) is the required integral formulation of total energy conservation in the moving coordinate system. It is seen from Equation (26) that the term $(\int_T \rho u_\alpha' d\tau') \frac{dV_\alpha}{dt}$ must be subtracted from the surface work term in order to make the present total energy conservation relation for a Eulerian coordinate system valid in the moving frame.

APPENDIX B

AFTON 2P FINITE DIFFERENCE EQUATIONS AT INTERIOR MESH POINTS RELATIVE TO A MOVING COORDINATE SYSTEM

Based on Equations (21), (22), (23), and (26) of Appendix A, the AFTON 2P finite difference equations for an Eulerian coordinate system may be converted to the moving coordinate system. The field of motion in AFTON 2P is actually covered with two closely related finite difference meshes -- one for the calculation of thermodynamic variables such as stress, i.e., quadrilateral zones, and the other for the calculation of kinematic variables like momentum, i.e., momentum zones.³ Figure 25 illustrates the two types of meshes in two space dimensions. The continuity and first law equations are applied to calculate properties on a quadrilateral zone while the equations of momentum and total energy conservation are used to calculate properties on a momentum zone. The finite difference equations relative to the moving coordinate system are as follows:

Definitions:

$\underline{R} = \underline{R}(x,y)$	Cartesian coordinate position relative to the moving frame
$\underline{U} = \underline{U}(u,v)$	material velocity relative to a coordinate point in the moving frame
E	internal energy
\hat{i}	unit vector in the x-direction (i.e., the plane of flow, and normal to the free stream flow relative to the laboratory frame)
H	total energy
\dot{W}	rate of work
\underline{V}_c	velocity of the moving frame relative to the laboratory frame
ρ	material density
\hat{k}	unit vector normal to (x,y) plane
m	mass
V	volume
\underline{M}	momentum

μ	viscosity
Δt	timestep
γ	ratio of specific heats
P	fluid pressure
$\sigma'_x, \sigma'_y, \tau'_{xy}$	viscous stresses
P	$\begin{pmatrix} P & 0 \\ 0 & P \end{pmatrix}$
σ''	$\begin{pmatrix} \sigma'_x & \tau'_{xy} \\ \sigma'_{xy} & \sigma'_y \end{pmatrix}$
σ	$P - \sigma''$
$\Delta x(t)$	displacement in the x-direction of the moving coordinate system relative to the laboratory frame (displacement of cylinder relative to laboratory frame)
A	amplitude of cylinder displacement
ω	frequency of cylinder displacement

Equations:

$$\Delta x = A \sin \omega t \quad (27)$$

$$\underline{v}_c = \hat{i} \omega A \cos \omega t \quad (28)$$

$$\frac{d\underline{v}_c}{dt} = \hat{i} A \omega^2 \sin \omega t \quad (29)$$

$$\underline{R} = \underline{R}^1 = \underline{R}^0 \quad (30)$$

$$\underline{U} = U(u, v) \quad (31)$$

$$\underline{A}_{12} = (\underline{R}_1 - \underline{R}_2) \times \hat{k} \quad (32)$$

$$\underline{A}_{32} = (\underline{R}_3 - \underline{R}_2) \times \hat{k} \quad (33)$$

$$W_{12} = \frac{1}{2}(\underline{U}_1 + \underline{U}_2) \quad (34)$$

$$\underline{W}_{32} = \frac{1}{2}(\underline{U}_3 + \underline{U}_2) \quad (35)$$

$$(\rho WA)_{12} = \rho_{12} \dot{\underline{W}}_{12} \cdot \underline{A}_{12} \quad (36)$$

$$(\rho WA)_{32} = \rho_{32} \dot{\underline{W}}_{32} \cdot \underline{A}_{32} \quad (37)$$

$$V = V^1 = V^0 \quad (38)$$

$$m^1 = m^0 + \Delta t [-(\rho WA)_{12} + (\rho WA)_{32} + (\rho WA)_{43} - (\rho WA)_{41}] \quad (39)$$

$$\rho^1 = m^1 / V \quad (40)$$

$$d_{ix} = x_i (y_{i-1} - y_{i+2}) + x_{i-1} (y_{i+2} - y_i) + x_{i+2} (y_i - y_{i-1}) \quad (41)$$

where: $i=1,2,3,4$ and, for example, when $i=1$, $i-1=4$

$$d_{iy} = -d_{ix} \quad (42)$$

$$A_{ix} = \frac{1}{2} \left[(y_{i-1} - y_{i+2}) / d_{ix} + (y_{i-1} - y_{i+1}) / d_{i+1 x} + (y_{i+2} - y_{i-1}) / d_{i+2 x} \right] \quad (43)$$

$$A_{iy} = \frac{1}{2} \left[(x_{i-1} - x_{i+2}) / d_{iy} + (x_{i-1} - x_{i-1}) / d_{i+1 y} + (x_{i+2} - x_{i-1}) / d_{i+2 y} \right] \quad (44)$$

$$\frac{\partial u}{\partial x} = A_{1x} u_1 + A_{2x} u_2 + A_{3x} u_3 + A_{4x} u_4 \quad (45)$$

$$\frac{\partial u}{\partial y} = A_{1y} u_1 + A_{2y} u_2 + A_{3y} u_3 + A_{4y} u_4 \quad (46)$$

$$\frac{\partial v}{\partial x} = A_{1x} v_1 + A_{2x} v_2 + A_{3x} v_3 + A_{4x} v_4 \quad (47)$$

$$\frac{\partial v}{\partial y} = A_{1y} v_1 + A_{2y} v_2 + A_{3y} v_3 + A_{4y} v_4 \quad (48)$$

$$\sigma_x = \mu \left[\frac{2}{3} \frac{\partial v}{\partial y} - \frac{4}{3} \frac{\partial u}{\partial x} \right] \quad (49)$$

$$\sigma_y = \mu \left[\frac{2}{3} \frac{\partial u}{\partial x} - \frac{4}{3} \frac{\partial v}{\partial y} \right] \quad (50)$$

$$\tau_{xy} = -\mu \left[\frac{\partial u}{\partial y} + \frac{\partial v}{\partial x} \right] \quad (51)$$

$$\tilde{P} = (\gamma - 1) \rho^1 E^0 \quad (52)$$

$$\underline{A}_{42} = \frac{1}{2} (\underline{R}_4 - \underline{R}_2) \times \hat{k} \quad (53)$$

$$\tilde{\underline{F}}_{42} = (\sigma^0 + P^0 - \sigma^1) \cdot \underline{A}_{42} \quad (54)$$

$$(\rho WAE)_{12} = (\rho WA)_{12} E_{12} \quad (55)$$

$$E_t = -(\rho WAE)_{12} + (\rho WAE)_{32} + (\rho WAE)_{43} - (\rho WAE)_{41} \quad (56)$$

$$\tilde{E} = \left[m^0 E^0 - (\tilde{\underline{F}}_{42} \cdot \underline{U}_1 + \tilde{\underline{F}}_{13} \cdot \underline{U}_2 + \tilde{\underline{F}}_{24} \cdot \underline{U}_3 + \tilde{\underline{F}}_{31} \cdot \underline{U}_4 - E_t) \Delta t \right] / m^1 \quad (57)$$

$$\tilde{\tilde{P}} = (\gamma - 1) \rho^1 \tilde{E} \quad (58)$$

$$\tilde{\tilde{\underline{F}}}_{42} = \frac{1}{2} (P^0 - \tilde{P}) \cdot \underline{A}_{42} \quad (59)$$

$$\tilde{\tilde{E}} = \tilde{E} - \left[\Delta t \cdot (\tilde{\tilde{\underline{F}}}_{42} \cdot \underline{U}_1 + \tilde{\tilde{\underline{F}}}_{13} \cdot \underline{U}_2 + \tilde{\tilde{\underline{F}}}_{24} \cdot \underline{U}_3 + \tilde{\tilde{\underline{F}}}_{31} \cdot \underline{U}_4) \right] / m^1 \quad (60)$$

$$P = (\gamma - 1) \rho^1 \tilde{\tilde{E}} \quad (61)$$

$$\underline{F}_{42} = \frac{1}{2} (\sigma^0 + \sigma^1) \cdot \underline{A}_{42} \quad (62)$$

$$\underline{E}^1 = \left[m^0 \underline{E}^0 - (\underline{F}_{42} \cdot \underline{U}_1 + \underline{F}_{13} \cdot \underline{U}_2 + \underline{F}_{24} \cdot \underline{U}_3 + \underline{F}_{31} \cdot \underline{U}_4) \Delta t \right] / m^1 \quad (63)$$

$$m_p^1 = \frac{1}{2} (m_a^1 + m_b^1 + m_c^1 + m_d^1) \quad (64)$$

$$\begin{aligned} \underline{M}_t^1 &= \frac{1}{2} \left[(\rho W A)_{42} + (\rho W A)_{12} + (\rho W A)_{54} + (\rho W A)_{61} \right] \cdot \frac{1}{2} (\underline{U}_4 + \underline{U}_1) \\ &+ \frac{1}{2} \left[(\rho W A)_{12} + (\rho W A)_{89} + (\rho W A)_{61} + (\rho W A)_{78} \right] \cdot \frac{1}{2} (\underline{U}_1 + \underline{U}_8) \\ &+ \frac{1}{2} \left[(\rho W A)_{56} + (\rho W A)_{41} + (\rho W A)_{67} + (\rho W A)_{18} \right] \cdot \frac{1}{2} (\underline{U}_6 + \underline{U}_1) \\ &+ \frac{1}{2} \left[(\rho W A)_{41} + (\rho W A)_{32} + (\rho W A)_{18} + (\rho W A)_{29} \right] \cdot \frac{1}{2} (\underline{U}_1 + \underline{U}_2) \end{aligned} \quad (65)$$

$$\underline{M}^1 = \underline{M}^0 + (\underline{F}_{42} + \underline{F}_{64} + \underline{F}_{86} + \underline{F}_{28} + \underline{M}_t) \Delta t - m_p^1 \frac{dVc}{dt} \Delta t \quad (66)$$

$$\underline{U} = (2\underline{M}^1 / m_p^1) - \underline{U} \quad (67)$$

$$H^1 = \frac{1}{2} m_p^1 (\underline{U}_1 \cdot \underline{U}_1) + \frac{1}{2} (m_a^1 E_a^1 + m_b^1 E_b^1 + m_c^1 E_c^1 + m_d^1 E_d^1) \quad (68)$$

$$\underline{F}_{ad} = \underline{P} \cdot (\underline{R}_a - \underline{R}_d) \times \hat{k} \quad (69)$$

$$\begin{aligned} \dot{W} &= - \left[\frac{1}{2} (\underline{U}_1 + \underline{U}_6) \cdot (\underline{F}_{bb} + \underline{F}_{bc}) + \frac{1}{2} (\underline{U}_1 + \underline{U}_8) \cdot (\underline{F}_{cc} + \underline{F}_{cd}) \right. \\ &\left. + \frac{1}{2} (\underline{U}_1 + \underline{U}_2) \cdot (\underline{F}_{dd} + \underline{F}_{da}) + \frac{1}{2} (\underline{U}_1 + \underline{U}_4) \cdot (\underline{F}_{aa} + \underline{F}_{ab}) \right] \end{aligned} \quad (70)$$

$$\begin{aligned} H_E &= \frac{1}{2} \left[(\rho W A E)_{43} + (\rho W A E)_{12} + (\rho W A E)_{59} + (\rho W A E)_{61} \right] \\ &+ \frac{1}{2} \left[(\rho W A E)_{12} + (\rho W A E)_{89} + (\rho W A E)_{61} + (\rho W A E)_{78} \right] \\ &+ \frac{1}{2} \left[(\rho W A E)_{56} + (\rho W A E)_{41} + (\rho W A E)_{67} + (\rho W A E)_{18} \right] \\ &+ \frac{1}{2} \left[(\rho W A E)_{41} + (\rho W A E)_{32} + (\rho W A E)_{18} + (\rho W A E)_{29} \right] \end{aligned} \quad (71)$$

$$\begin{aligned}
H_{KE} &= \frac{1}{16} \left[(\rho WA)_{43} + (\rho WA)_{12} + (\rho WA)_{54} + (\rho WA)_{61} \right] (\underline{U}_4 + \underline{U}_1)^2 \\
&+ \frac{1}{16} \left[(\rho WA)_{12} + (\rho WA)_{89} + (\rho WA)_{61} + (\rho WA)_{78} \right] (\underline{U}_1 + \underline{U}_8)^2 \\
&+ \frac{1}{16} \left[(\rho WA)_{56} + (\rho WA)_{41} + (\rho WA)_{67} + (\rho WA)_{18} \right] (\underline{U}_6 + \underline{U}_1)^2 \\
&+ \frac{1}{16} \left[(\rho WA)_{41} + (\rho WA)_{32} + (\rho WA)_{18} + (\rho WA)_{29} \right] (\underline{U}_1 + \underline{U}_2)^2
\end{aligned} \tag{72}$$

$$\begin{aligned}
\dot{W} &= - \left[\frac{1}{2} (\underline{U}_1 + \underline{U}_6) \cdot (\underline{F}_{bb} + \underline{F}_{bc}) + \frac{1}{2} (\underline{U}_1 + \underline{U}_8) \cdot (\underline{F}_{cc} + \underline{F}_{cd}) \right. \\
&\quad \left. + \frac{1}{2} (\underline{U}_1 + \underline{U}_2) \cdot (\underline{F}_{dd} + \underline{F}_{da}) + \frac{1}{2} (\underline{U}_1 + \underline{U}_4) \cdot (\underline{F}_{aa} + \underline{F}_{ab}) \right]
\end{aligned} \tag{73}$$

$$H^1 = H^0 - \dot{W} \Delta t - \frac{dV_c}{dt} \cdot m_p^1 \underline{U} \Delta t - (H_E + H_{KE}) \Delta t \tag{74}$$

APPENDIX C

DOWNSTREAM AND LATERAL BOUNDARY CONDITIONS

The downstream and lateral characteristic boundary conditions used in this program were based on two principal assumptions, namely, that each streamline of the flow field in the neighborhood of the boundary at any instant of time constitutes a region of transient one-dimensional slab flow, and that the sound speed has its free stream value at the downstream boundary. For the case of the moving cylinder, this characteristic boundary condition was applied relative to a laboratory frame. The flow field variables can then be calculated at either the downstream or lateral boundaries as follows:

First, knowing the velocity field at an instant of time, the position of any particle can be updated by one timestep from an "earlier time" to a "later time". In particular, a particle position can be found at an earlier time such that one timestep later the particle will arrive at a given boundary mesh point. For this purpose the discrete velocity field is assumed constant during the timestep and is made spatially continuous by interpolation; we interpolated linearly. Thus, one can calculate the direction of the streamline along which that particle travels which arrives at the given boundary point at the later time. Let the boundary mesh point be denoted as point "B", and the particle position at the earlier time as point "P"; also, let the superscript "o" define a property at the earlier time, let the superscript "1" define a property at the later time, and let the absence of a superscript indicate a property defined at a time halfway between the earlier and the later times. Due to the transverse motion of the cylinder, the x-component u_c^o of the velocity of the moving coordinate system is given by

$$u_c^o = \omega A \cos \omega t \quad (75)$$

where A is the amplitude of the oscillation and ω is the frequency. The required streamline direction can be specified in terms of the components \bar{u} , \bar{v} of the average velocity vector (relative to the laboratory frame) between points B and P, as follows:

$$\bar{u} = \left[\left(1 + (\partial v / \partial y)^0 (\Delta t / 2) (u_B^0 + u_C^0) - (\partial u / \partial y)^0 v_B^0 (\Delta t / 2) \right) / g \right] \quad (76)$$

$$\bar{v} = \left[\left(1 + (\partial u / \partial x)^0 (\Delta t / 2) v_B^0 - (\partial v / \partial x)^0 (u_B^0 + u_C^0) (\Delta t / 2) \right) / g \right] \quad (77)$$

$$g = \left[1 + (\partial u / \partial x)^0 (\Delta t / 2) \right] \left[1 + (\partial v / \partial y)^0 (\Delta t / 2) \right] - (\partial v / \partial x)^0 (\partial u / \partial y)^0 (\Delta t / 2)^2 \quad (78)$$

where \bar{u} is the average velocity component in the x-direction, \bar{v} is the average velocity component in the y-direction, u_B^0 is the x-component of velocity at point B, v_B^0 is the y-component of velocity at point B, Δt is the time increment, and $(\partial u / \partial x)^0$, $(\partial v / \partial x)^0$, $(\partial u / \partial y)^0$ are the velocity derivatives evaluated at the zone centroid (see Appendix B). The direction cosines of the required streamline are then:

$$X_{DIR} = \bar{u} / \bar{U} \quad (79)$$

$$Y_{DIR} = \bar{v} / \bar{U} \quad (80)$$

where

$$\bar{U} = \sqrt{\bar{u}^2 + \bar{v}^2} \quad (81)$$

Assuming that sound signals travel along the streamline as in one-dimensional slab flow, it is also possible to calculate from the known earlier-time flow field both the particle velocity and the sound speed at a point S from which a sound signal would have to depart at the earlier time in order to reach the boundary point at the later time. Based on the

zone sound speed (which is assumed uniform in each zone) and the average velocity vector between points P and B, the location of the point S can be determined approximately from the following relations:

$$(x_S - x_B) = -(\bar{U} + C) X_{DIR} \Delta t \quad (82)$$

$$(y_S - y_B) = -(\bar{U} + C) Y_{DIR} \Delta t \quad (83)$$

where C is the zone sound speed. From the Equations (82), (83) and the discrete velocity field at the earlier time (i.e., time "o") the components of the velocity vector at point S at the earlier time are

$$u_S^o = u_B^o + u_c^o - (U + C) \Delta t \left[X_{DIR} (\partial u / \partial x)^o + Y_{DIR} (\partial u / \partial y)^o \right] \quad (84)$$

$$v_S^o = v_B^o - (\bar{U} + C) \Delta t \left[X_{DIR} (\partial v / \partial x)^o + Y_{DIR} (\partial v / \partial y)^o \right] \quad (85)$$

$$U_S^o = \sqrt{(v_S^o)^2 + (u_S^o + u_c^o)^2} \quad (86)$$

where u_S^o is the x-component of the velocity at S, v_S^o is the y-component of the velocity at S, and U_S^o is the magnitude of the velocity vector at S.

Based on the assumption that the sound speed has its free stream value at the downstream boundary point B, the sound speed at the point S can be determined at the earlier time by linear interpolation. For the downstream boundary, the relation is as follows:

$$C_S^o = C_\infty + 2 (\bar{U} + C) Y_{DIR} \Delta t \left(\frac{C - C_\infty}{y_B - y_A} \right) \quad (87)$$

At a lateral boundary Equation (87) is replaced by the equation

$$C_S^o = C_\infty + 2 (\bar{U} + C) X_{DIR} \Delta t \left(\frac{C - C_\infty}{x_B - x_A} \right) \quad (88)$$

where C_S^0 is the sound speed at S, C_∞ is the free stream sound speed, C is the sound speed of the zone containing the point S, and y_A is the y-coordinate of the interior mesh point "A" adjacent to the boundary point B.

According to the method of characteristics as applied to the one-dimensional linear isentropic flow of a polytropic gas, the Riemann variable

$$R = U + 2C/(\gamma-1) \quad (89)$$

is constant along any sound signal trajectory, where γ is the ratio of heat capacities for the gas. By hypothesis here, each streamline in the neighborhood of the downstream boundary is a region of one-dimensional, linear isentropic flow during a timestep of the numerical calculation. Hence, the Riemann variable R has the same value at the point S at time 0, as it has at the point B at time 1, namely

$$R = U_S^0 + 2C_S^0/(\gamma-1) \quad (90)$$

From the assumed free stream speed of sound at the boundary point B, and the known Riemann invariant, the particle velocity in the streamline direction can then be computed at the point B at the later time, as follows:

$$U_B^1 = U_S^0 + (C_S^0 - C_\infty)/(\gamma-1) \quad (91)$$

Assuming the direction of flow to be the same at times 0 and 1, the particle velocity can be found as a complete vector quantity according to the equations

$$u_B^1 = U_B^1 X_{DIR} \quad (92)$$

$$v_B^1 = U_B^1 Y_{DIR} \quad (93)$$

To complete this description of downstream boundary flow, mass and internal energy are transported across the boundary at the densities characteristic of the interior of the zone containing the point S. This boundary condition has now been applied downstream in many calculations of viscous compressible flow around obstacles, where it appears to provide a good approximation to flow out of the region of calculation.

APPENDIX D

NOMENCLATURE

a,	Cylinder radius
A,	Amplitude of oscillation of the cylinder
c,	Local speed of sound, $c = \sqrt{\frac{\gamma P}{\rho}}$
c_∞ ,	Free stream speed of sound, $c_\infty = \sqrt{\frac{\gamma P_\infty}{\rho_\infty}}$
C_D ,	Instantaneous drag coefficient, $C_D = \frac{\text{Drag}}{\frac{1}{2} \rho_\infty U_\infty^2 d}$
\bar{C}_D ,	Time-averaged drag coefficient, $\bar{C}_D = \frac{1}{T} \int_0^T C_D dt$
C_L ,	Instantaneous lift coefficient, $C_L = \frac{\text{Lift}}{\frac{1}{2} \rho_\infty U_\infty^2 d}$
\bar{C}_L ,	Time-averaged lift coefficient, $\bar{C}_L = \frac{1}{T} \int_0^T C_L dt$
$C_L(\text{r.m.s.})$,	Root mean square lift coefficient, $C_L(\text{r.m.s.}) = \left[\frac{1}{T} \int_0^T C_L^2 dt \right]^{\frac{1}{2}}$
$C_{L_0}(\text{r.m.s.})$,	Root mean square lift coefficient for a stationary cylinder
C_p ,	Local pressure coefficient, $C_p = \frac{P - P_\infty}{\frac{1}{2} \rho_\infty U_\infty^2}$
C_p ,	Specific heat at constant pressure
C_v ,	Specific heat at constant volume

d,	Cylinder diameter
M,	Mach number, $M = U/a$
M_∞ ,	Free stream Mach number, $M_\infty = U_\infty/c_\infty$
n,	Shedding frequency
P,	Pressure
P_∞ ,	Free stream pressure
P,	Riemann invariant, $P = \frac{2}{\gamma - 1} a + U$
R,	Reynolds number, $R = \frac{\rho U d}{\mu}$
s,	Arc length
S,	Strouhal number, $S = \frac{nd}{U}$
S_0 ,	Strouhal number for stationary cylinder
t,	Time
T,	Temperature
T,	Time integration interval for evaluation of time averages
u,	Local velocity component in the boundary layer parallel to the wall
U_∞ ,	Magnitude of free stream velocity vector
U,	Magnitude of local velocity vector

\underline{U} ,	Local velocity vector
x ,	Coordinate normal to free stream velocity vector
y ,	Coordinate parallel to free stream velocity vector
γ ,	Ratio of specific heats, $\gamma = C_p/C_v$
δ ,	Boundary layer thickness
ρ ,	Density
ϕ ,	Dimensionless cylinder oscillation frequency, $\phi = \frac{\omega d}{2\pi U_\infty}$
ρ_∞ ,	Free stream density
θ ,	Angle measured along the circumference of the cylinder from the forward stagnation point.
τ ,	Characteristic time; the number of cylinder diameters that a particle traveling with free stream velocity would move in a given time.
ω ,	Angular frequency of cylinder oscillation

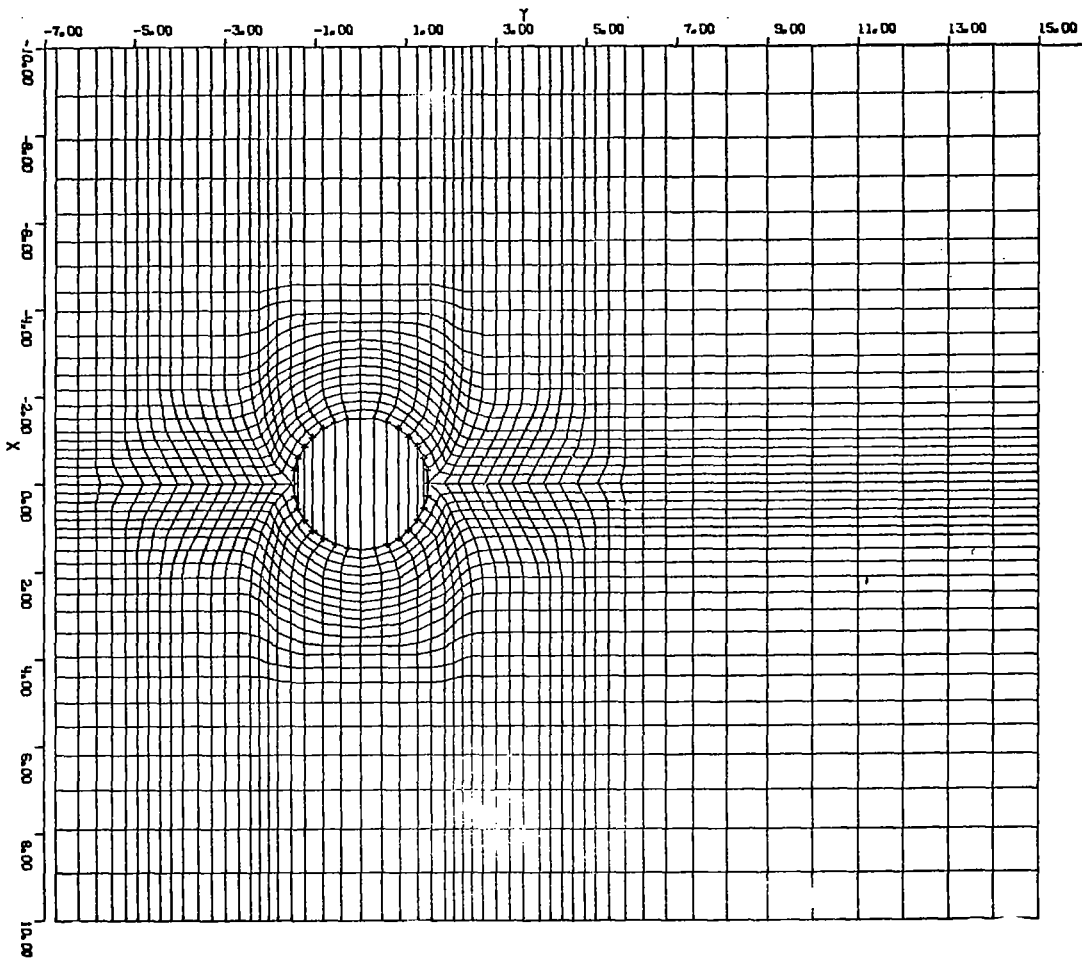


Figure 1. Finite difference mesh (43 x 80); This finite difference mesh has an upstream boundary located at $y = -20$ cm, although only the portion of the mesh downstream of $y = -7$ cm is indicated.

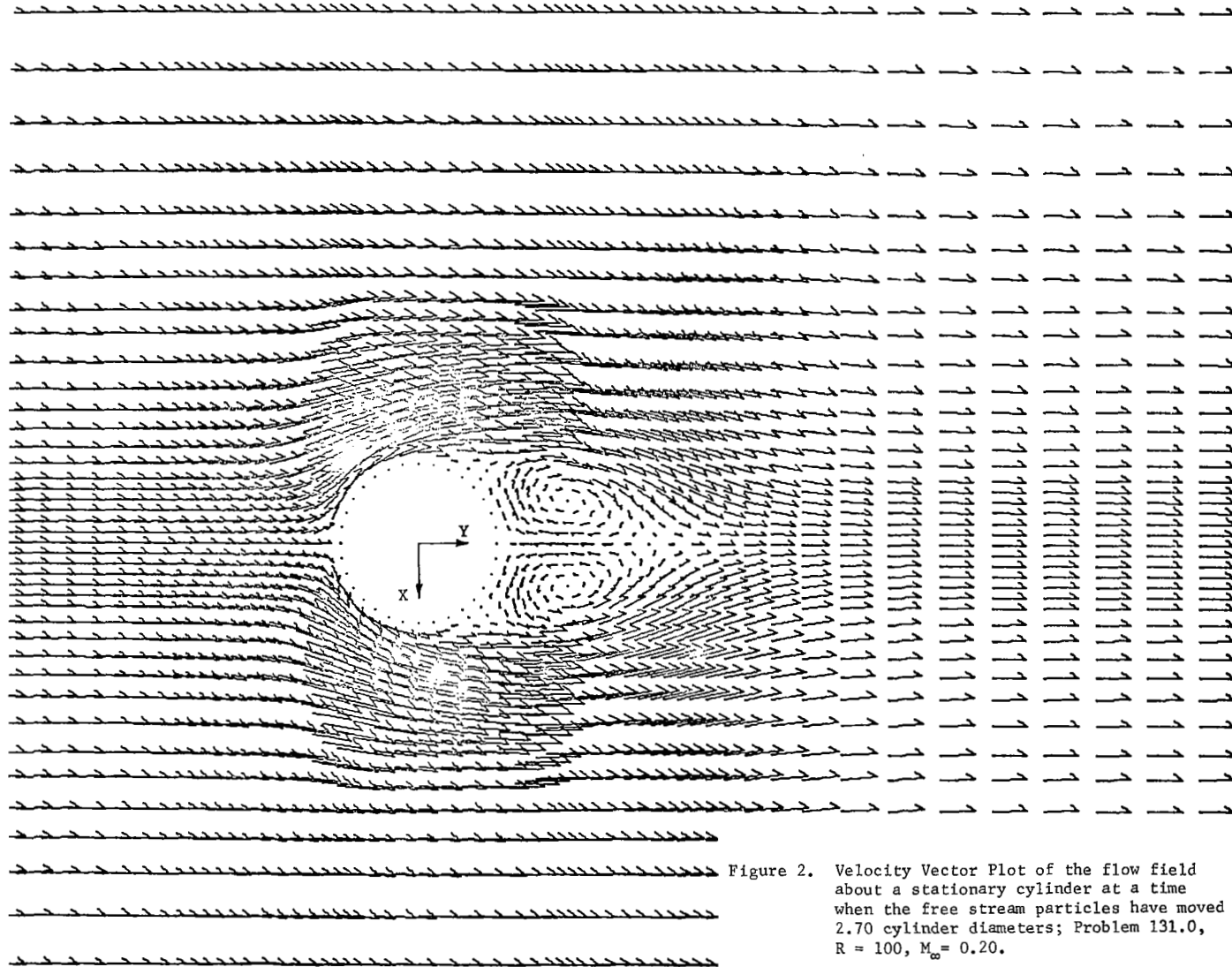


Figure 2. Velocity Vector Plot of the flow field about a stationary cylinder at a time when the free stream particles have moved 2.70 cylinder diameters; Problem 131.0, $R = 100$, $M_\infty = 0.20$.

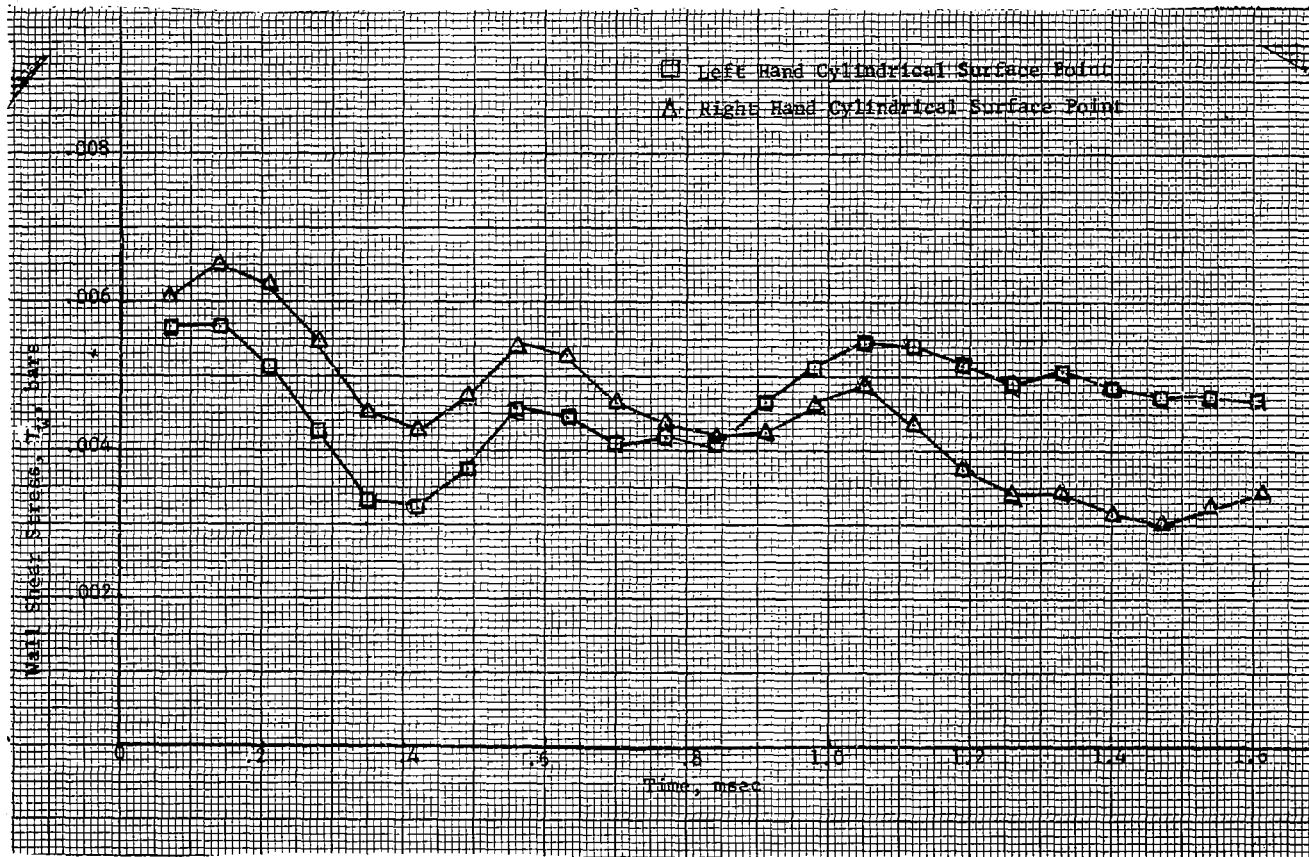


Figure 3

Wall shear stress distributions vs. time at points on the cylindrical surface, plus and minus 90 degrees from the forward stagnation point of the cylinder; Problem 133.0, $R = 100.0$, $M_{\infty} = 0.20$; time is measured from the start of cylinder motion, i.e., 1.19 msec after the start of motion.

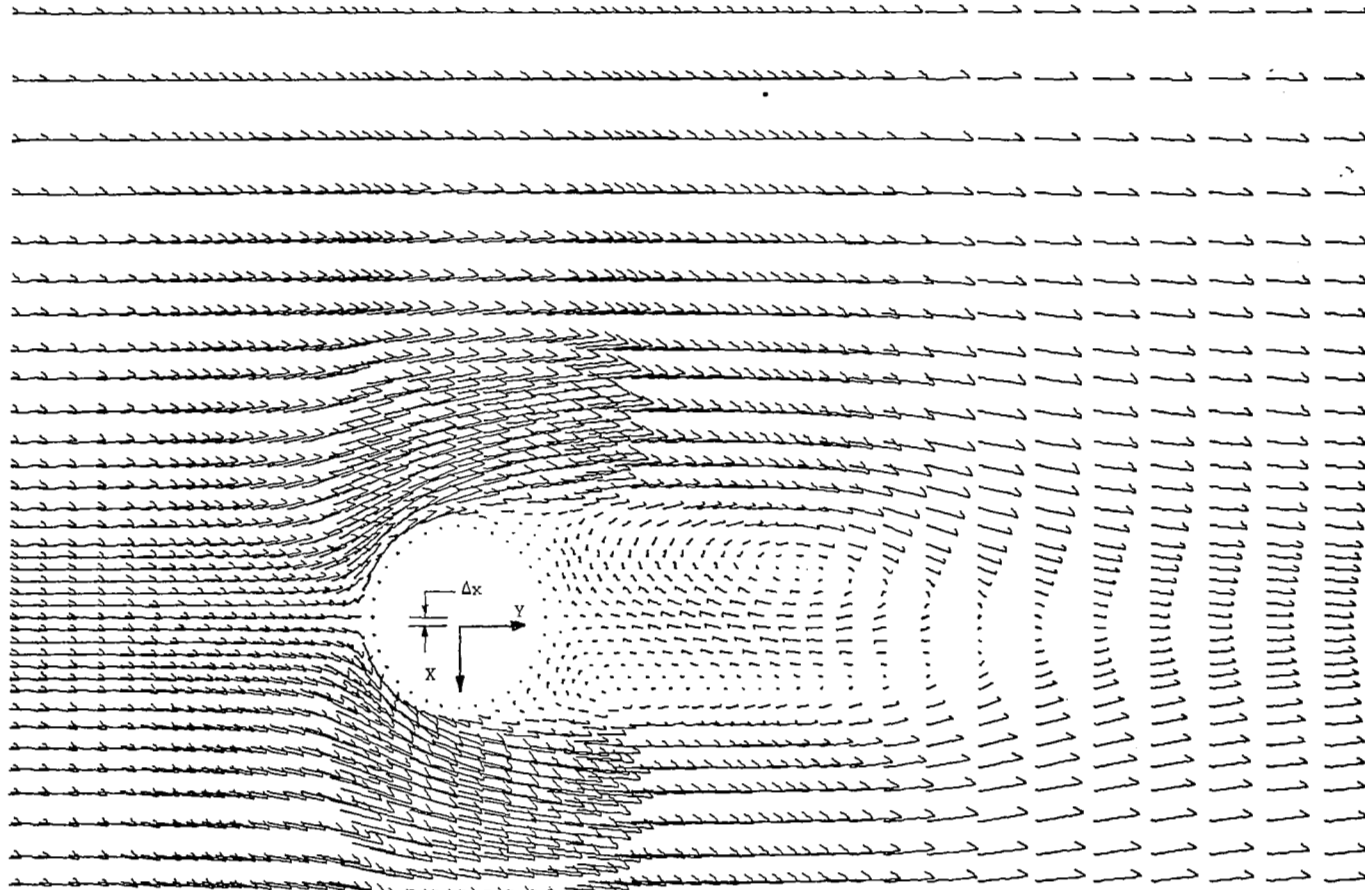


Figure 5. Velocity Vector Plot of the Moving Cylinder Flow Field at a time when the free stream particles have moved 7.95 cylinder diameters; Problem 133.0, $R = 100$, $M_{\infty} = 0.20$; Oscillation frequency 2.42 radius/msec, Oscillation amplitude 10% of cylinder radius.

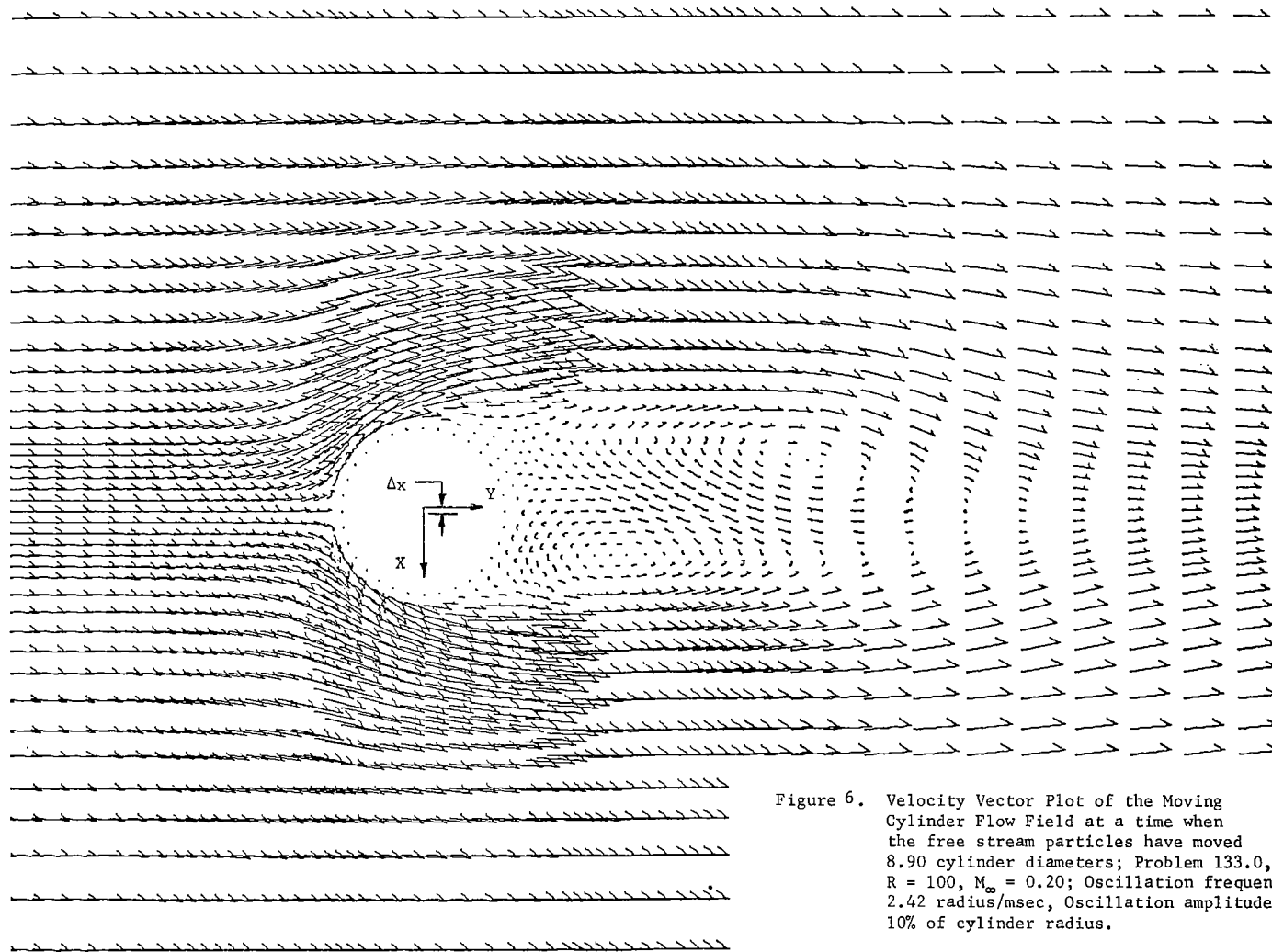


Figure 6. Velocity Vector Plot of the Moving Cylinder Flow Field at a time when the free stream particles have moved 8.90 cylinder diameters; Problem 133.0, $R = 100$, $M_\infty = 0.20$; Oscillation frequency 2.42 radius/msec, Oscillation amplitude 10% of cylinder radius.

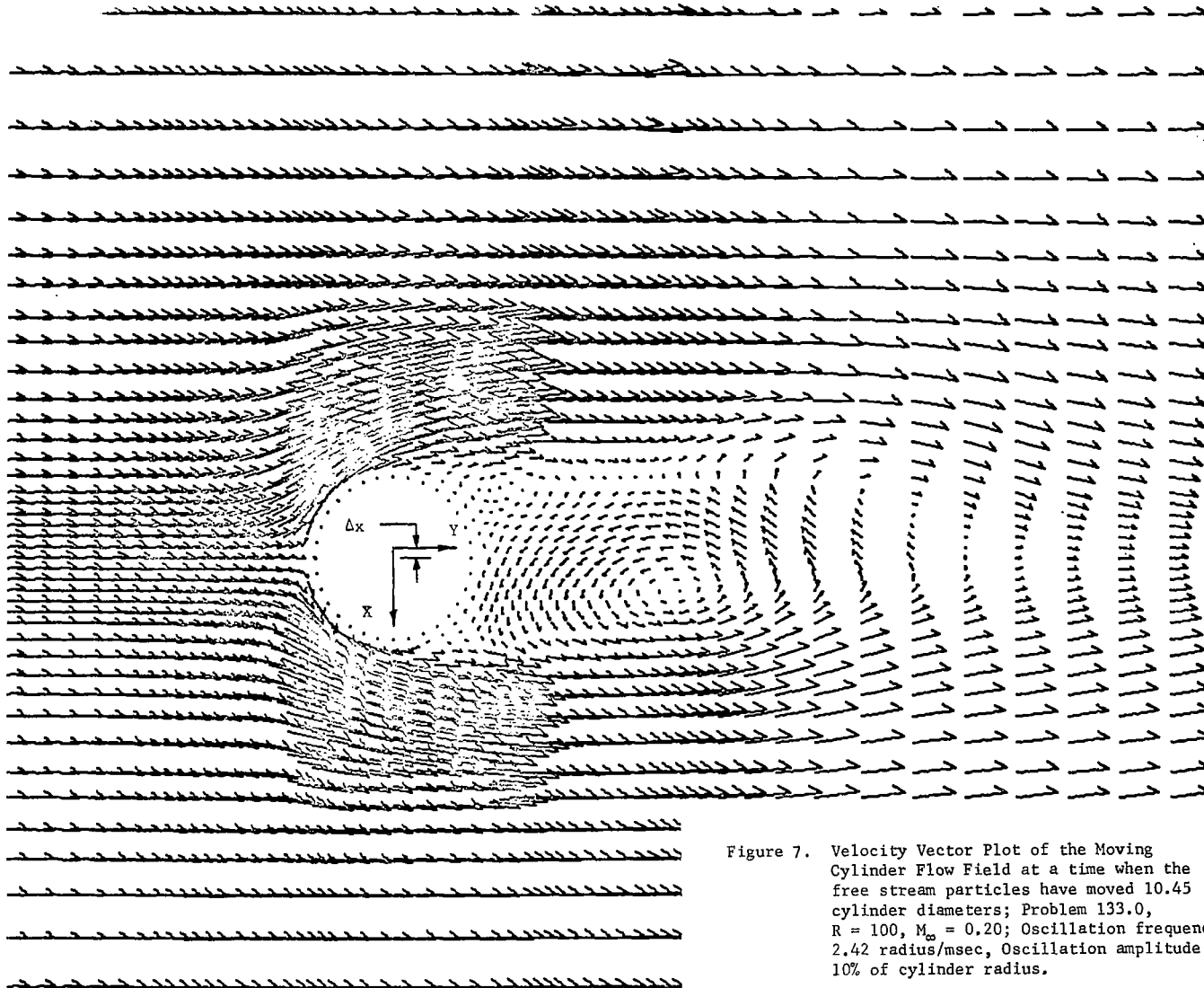


Figure 7. Velocity Vector Plot of the Moving Cylinder Flow Field at a time when the free stream particles have moved 10.45 cylinder diameters; Problem 133.0, $R = 100$, $M_\infty = 0.20$; Oscillation frequency 2.42 radius/msec, Oscillation amplitude 10% of cylinder radius.

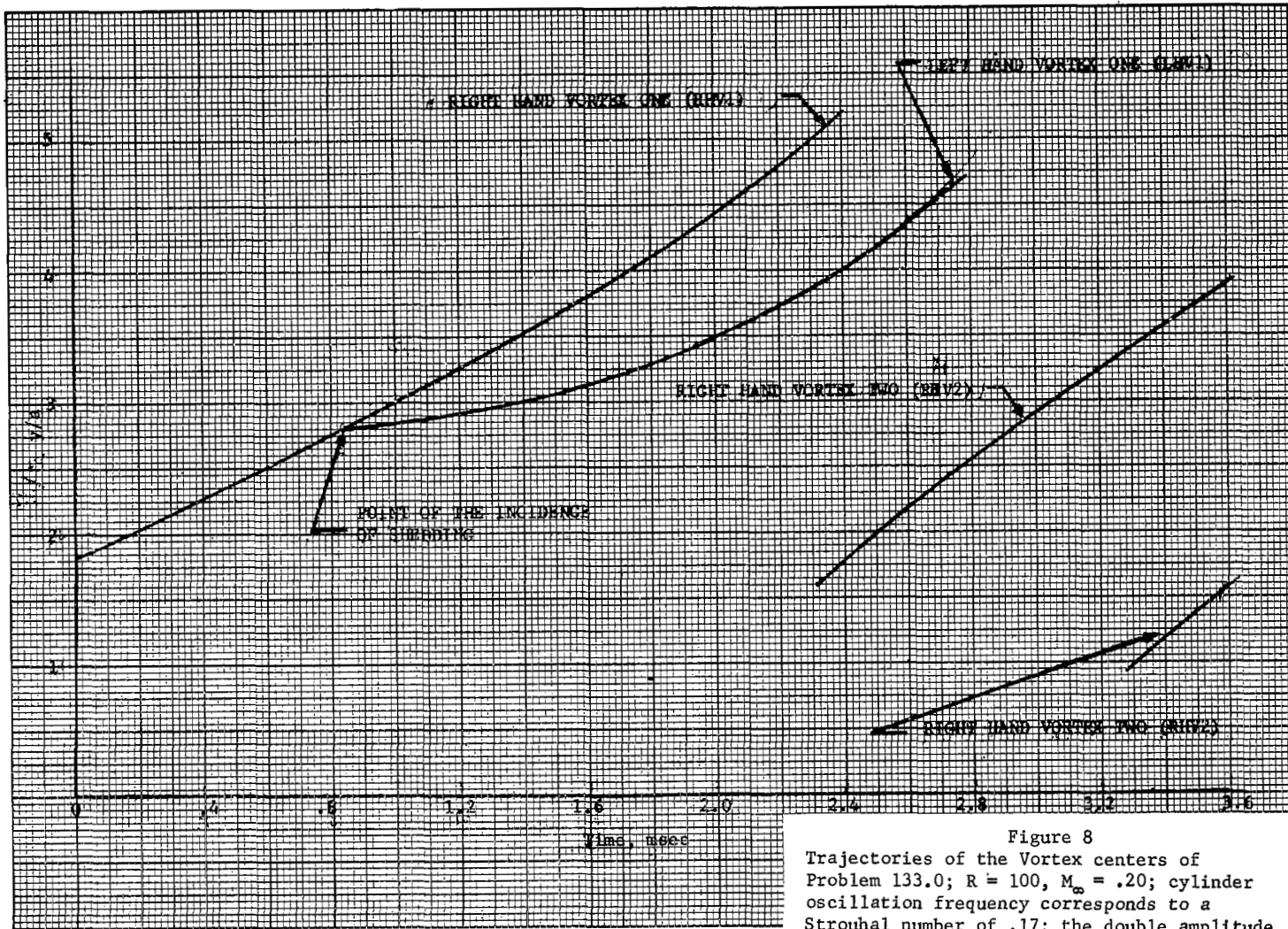


Figure 8
 Trajectories of the Vortex centers of
 Problem 133.0; $R = 100$, $M_\infty = .20$; cylinder
 oscillation frequency corresponds to a
 Strouhal number of .17; the double amplitude
 is 10% of the cylinder diameter.

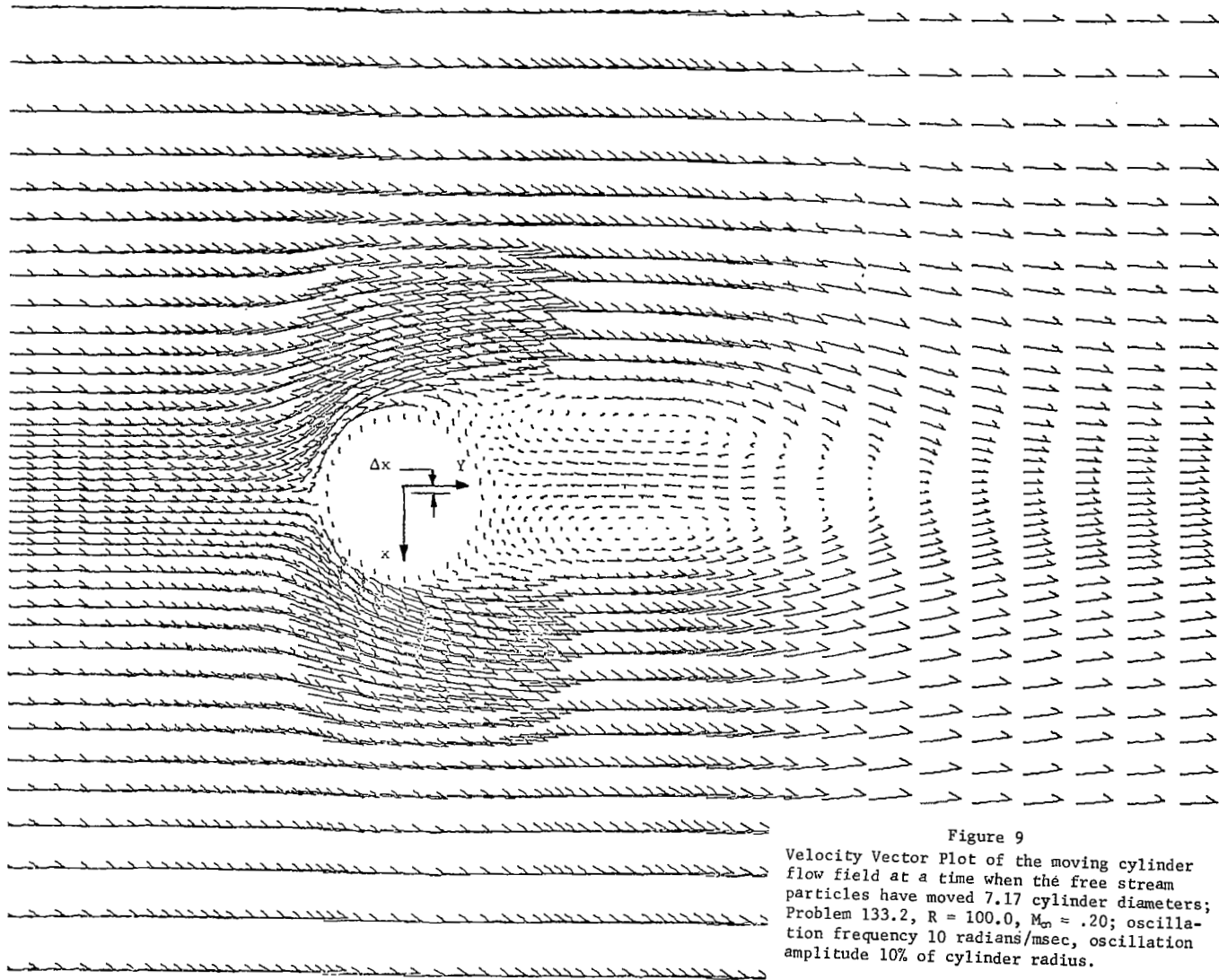


Figure 9
Velocity Vector Plot of the moving cylinder
flow field at a time when the free stream
particles have moved 7.17 cylinder diameters;
Problem 133.2, $R = 100.0$, $M_\infty \approx .20$; oscillation
frequency 10 radians/msec, oscillation
amplitude 10% of cylinder radius.

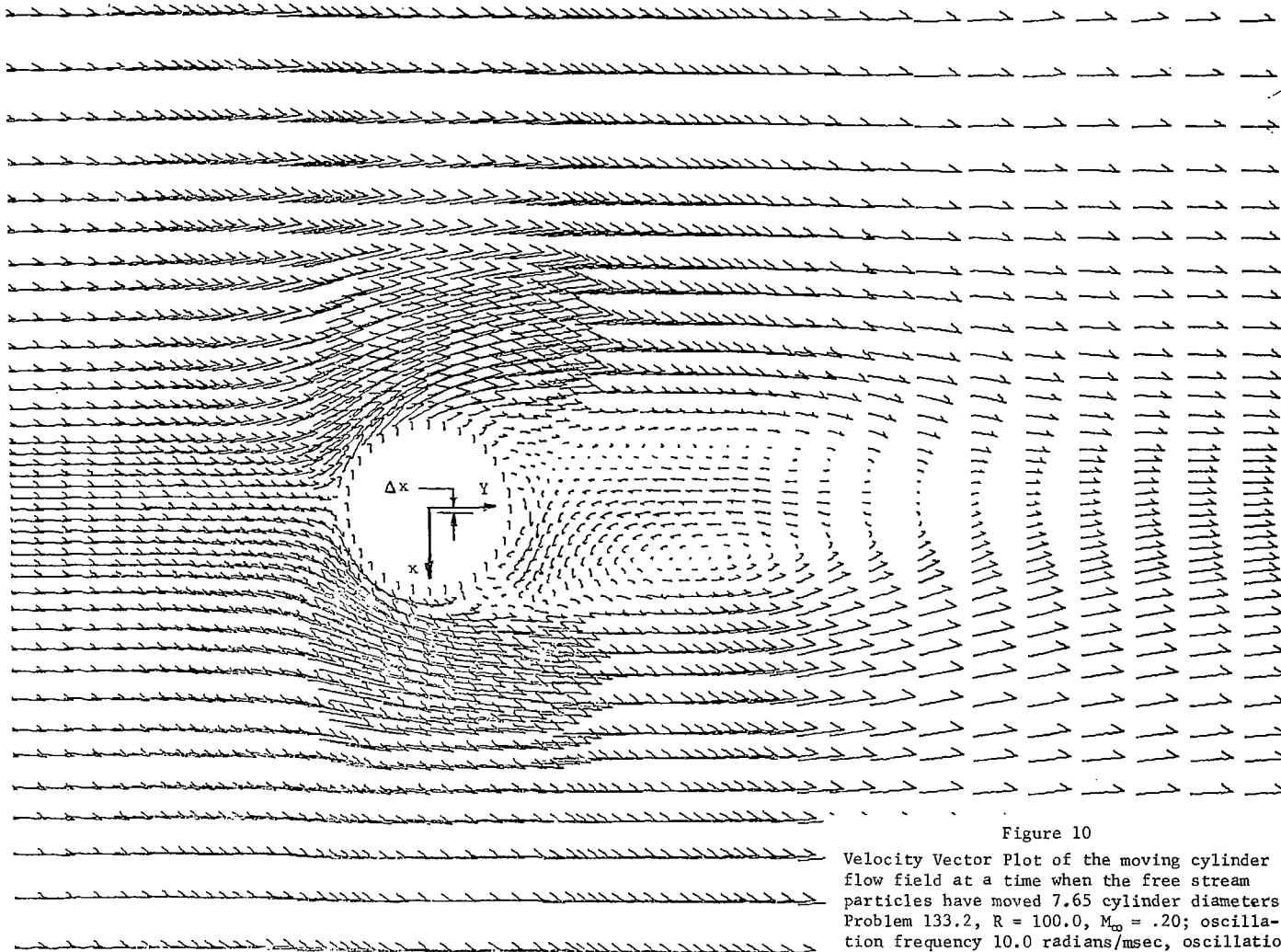
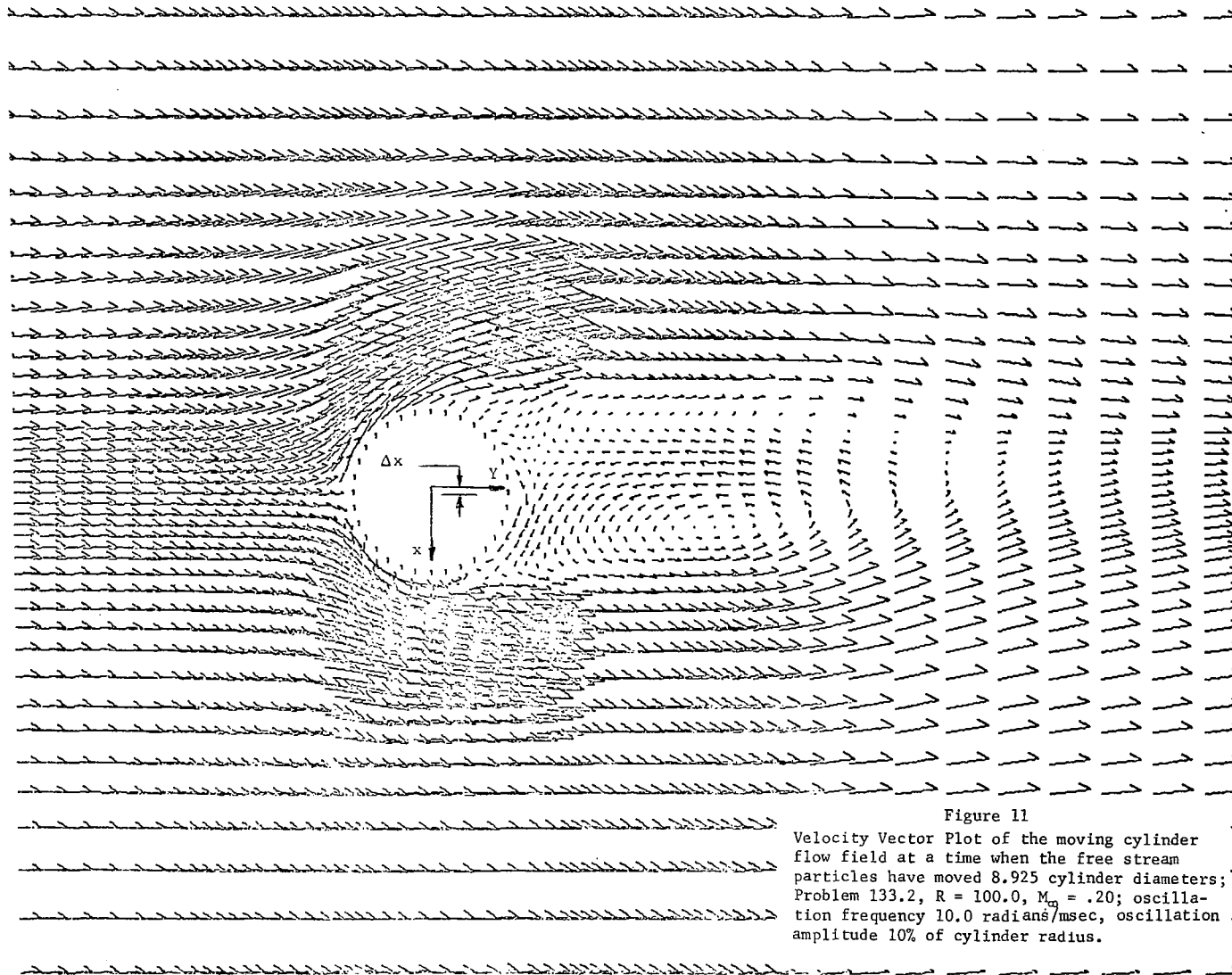


Figure 10

Velocity Vector Plot of the moving cylinder flow field at a time when the free stream particles have moved 7.65 cylinder diameters; Problem 133.2, $R = 100.0$, $M_\infty = .20$; oscillation frequency 10.0 radians/msec, oscillation amplitude 10% of cylinder radius.



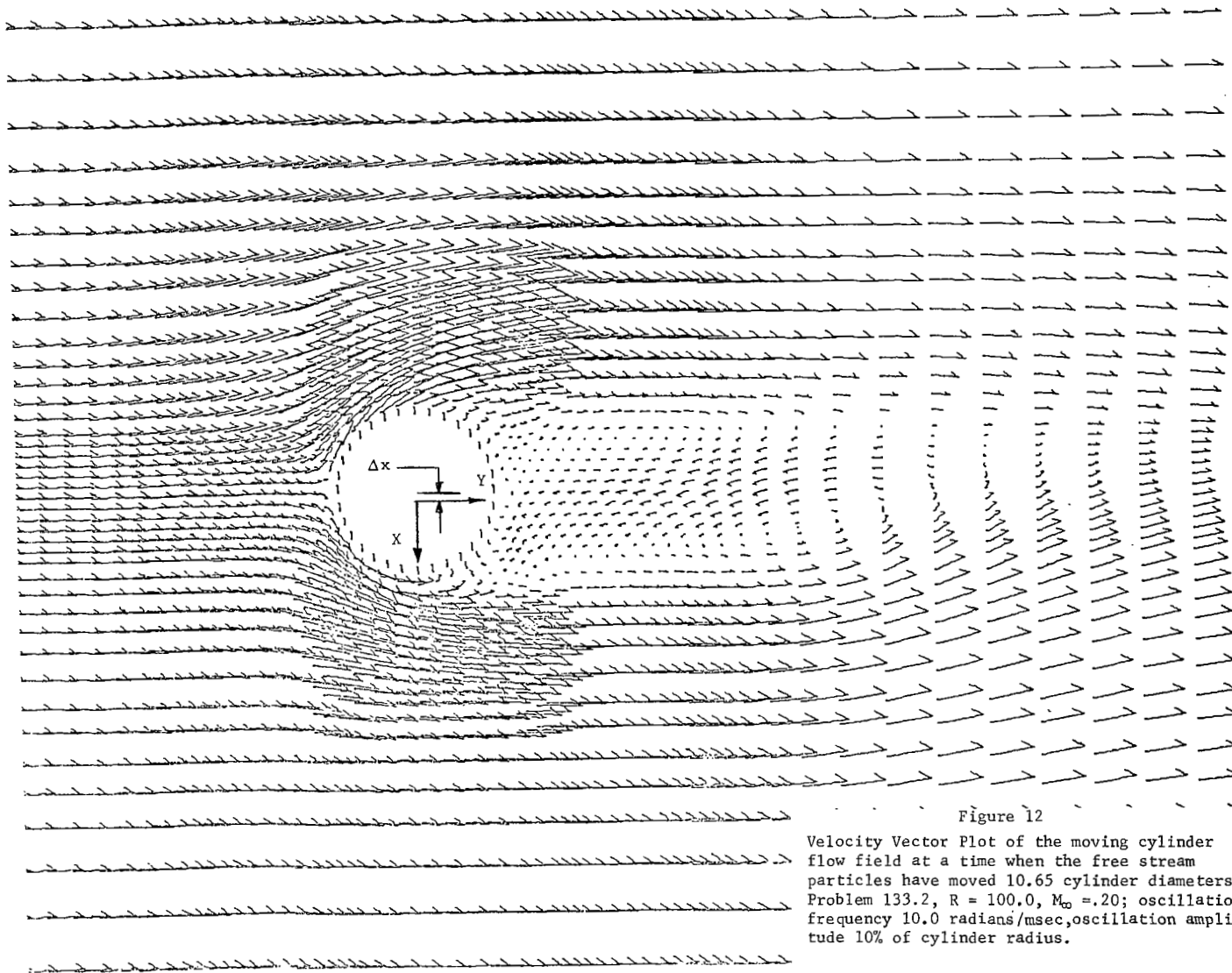


Figure 12

Velocity Vector Plot of the moving cylinder flow field at a time when the free stream particles have moved 10.65 cylinder diameters; Problem 133.2, $R = 100.0$, $M_{\infty} = .20$; oscillation frequency 10.0 radians/msec, oscillation amplitude 10% of cylinder radius.

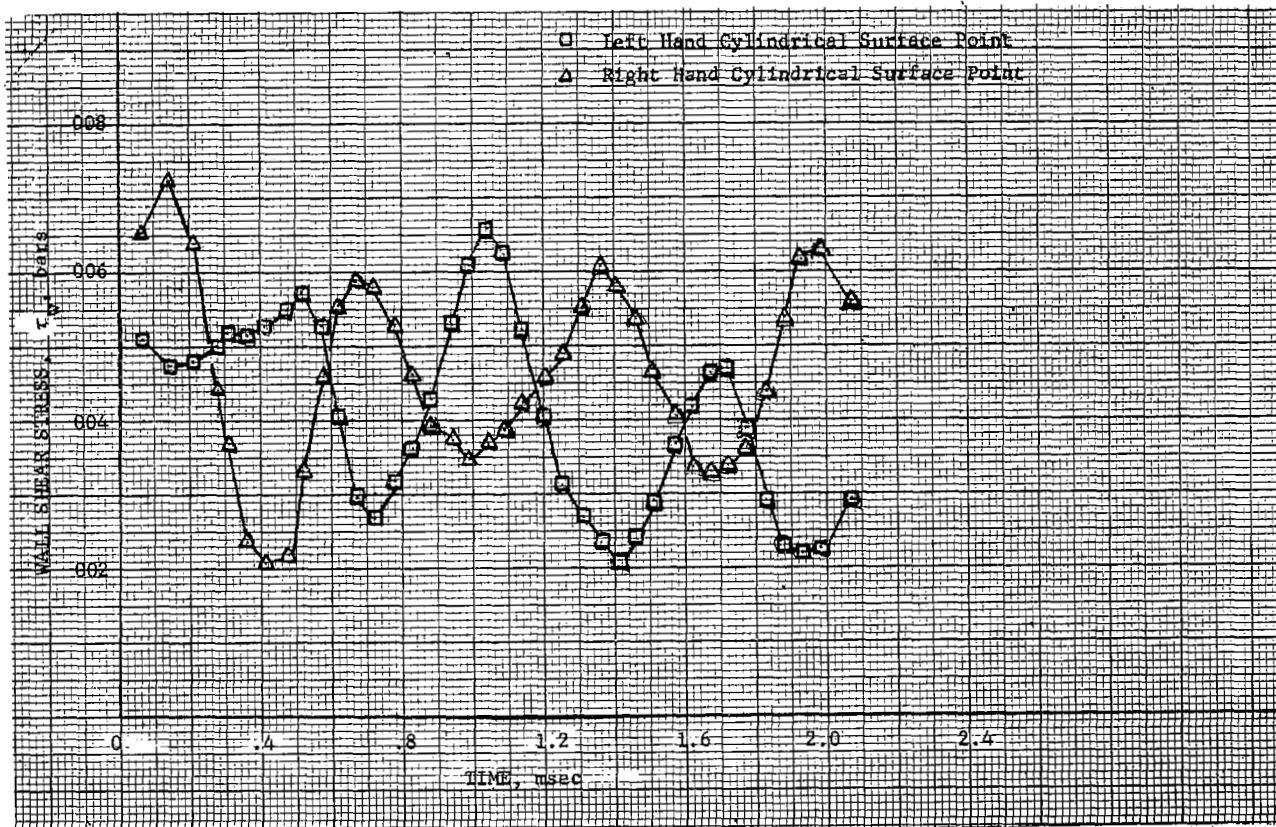


Figure 13
 Wall shear stress distributions, vs. time at points on the cylindrical surface plus and minus 90 degrees from the forward stagnation point; Problem 133.2, $R = 100.0$, $M_\infty = .20$; time is measured from the start of cylinder motion, i.e., 1.19 msec after the start of motion.

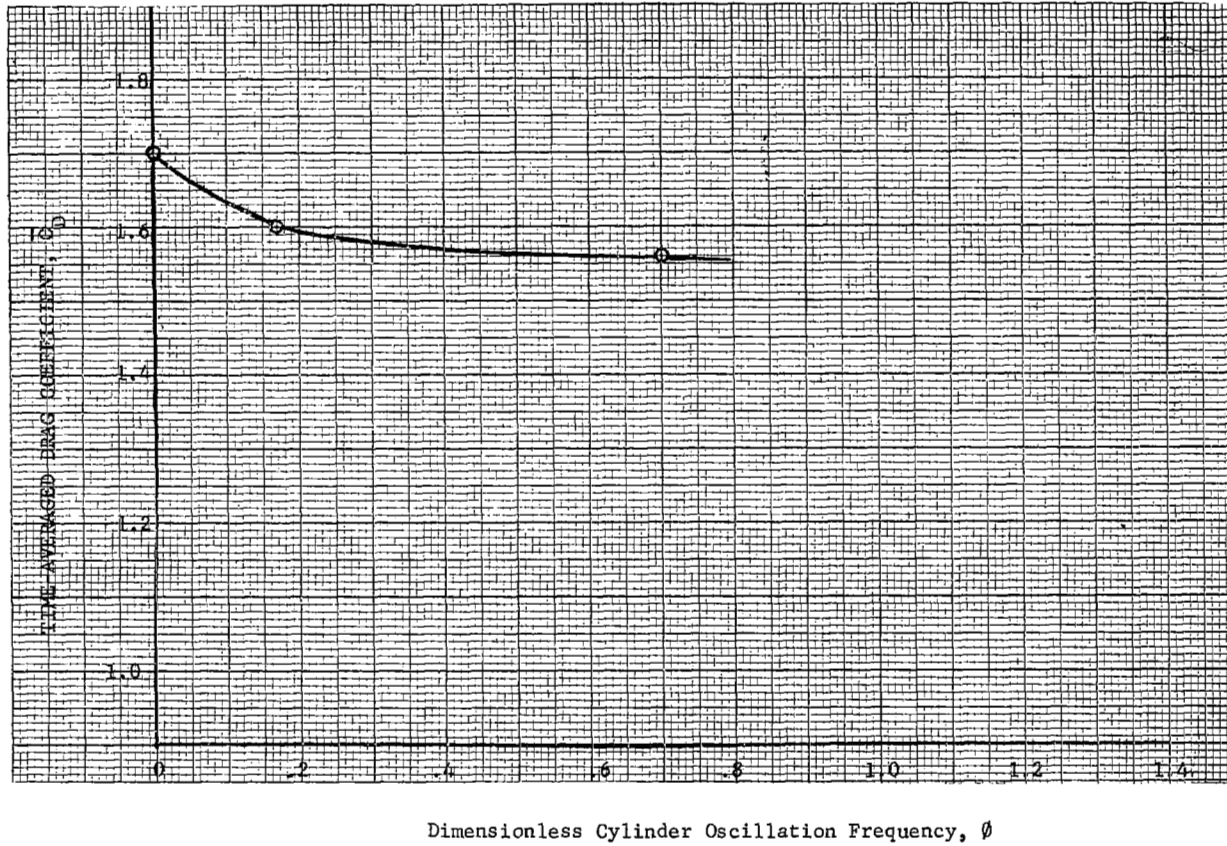


Figure 14
Time-averaged drag coefficient variation
with dimensionless cylinder oscillation
frequency; $R = 100.0$, $M_\infty = 0.20$; cylinder
oscillation double amplitude 10% of the
cylinder diameter.

STROUHAL NUMBER, S

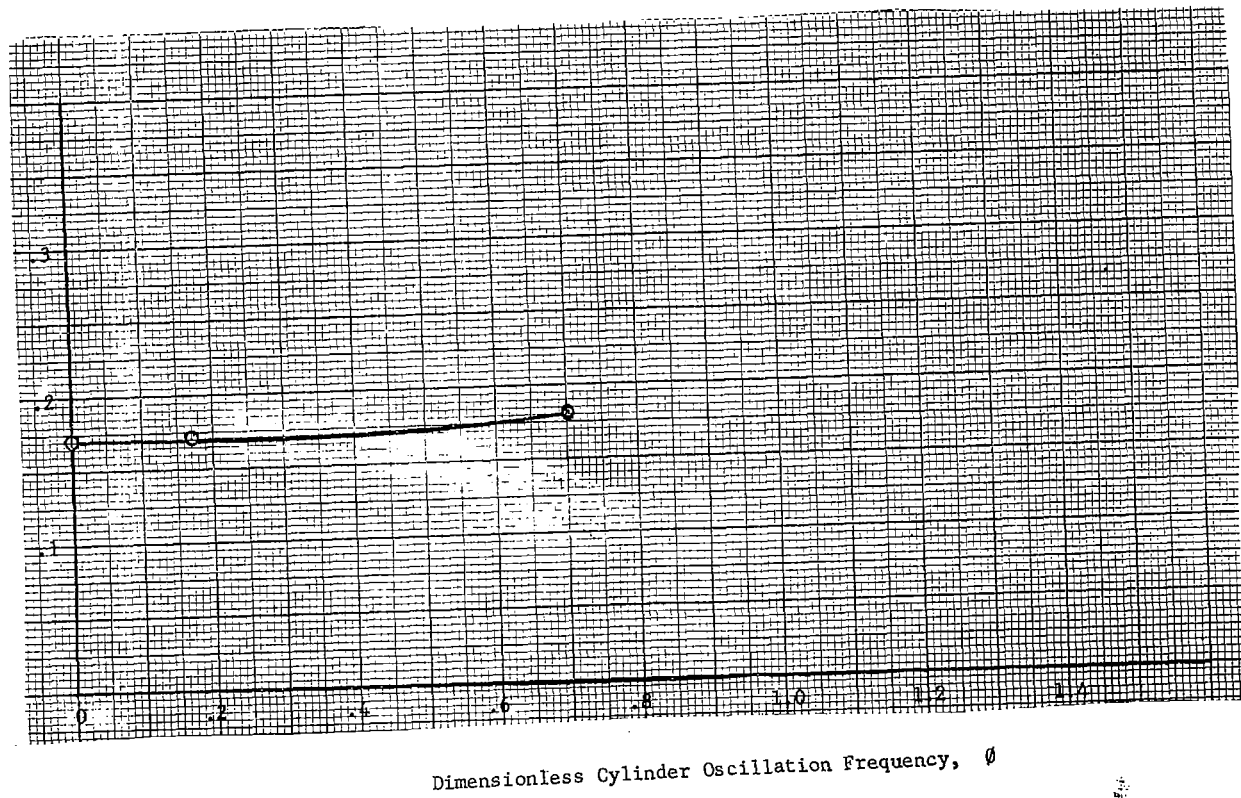
Dimensionless Cylinder Oscillation Frequency, ϕ

Figure 15
Strouhal number variation with dimensionless
cylinder oscillation frequency; $R = 100.0$,
 $M_\infty = 0.2$; double oscillation amplitude equal
to 10% of the cylinder diameter.

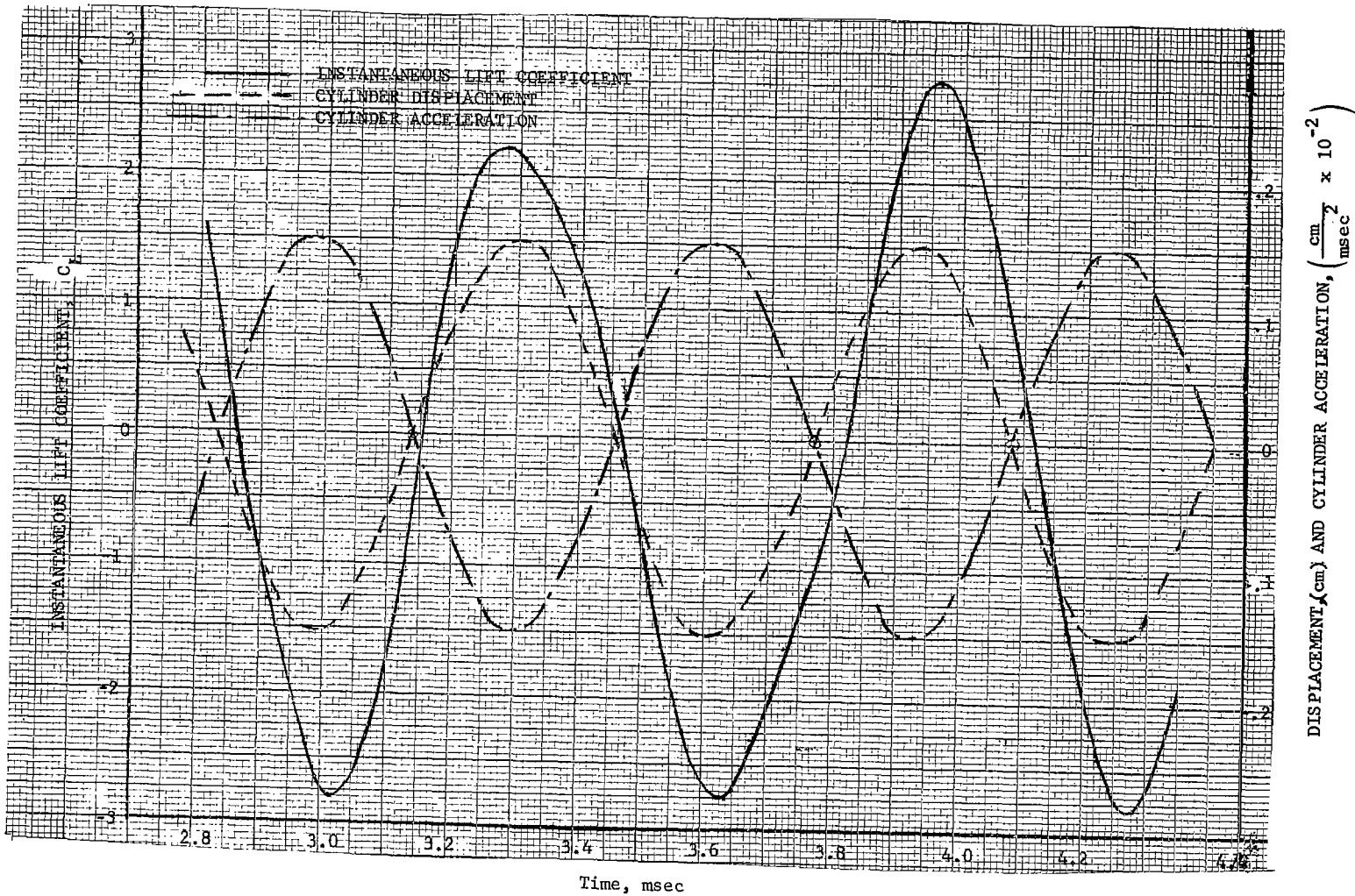


Figure 16
 Instantaneous lift coefficient cylinder
 acceleration and cylinder displacement varia-
 tions with time; Problem 133.2; time measured
 from the start of the cylinder oscillation.

DISPLACEMENT (cm) AND CYLINDER ACCELERATION, $\left(\frac{\text{cm}}{\text{msec}^2} \times 10^{-2}\right)$

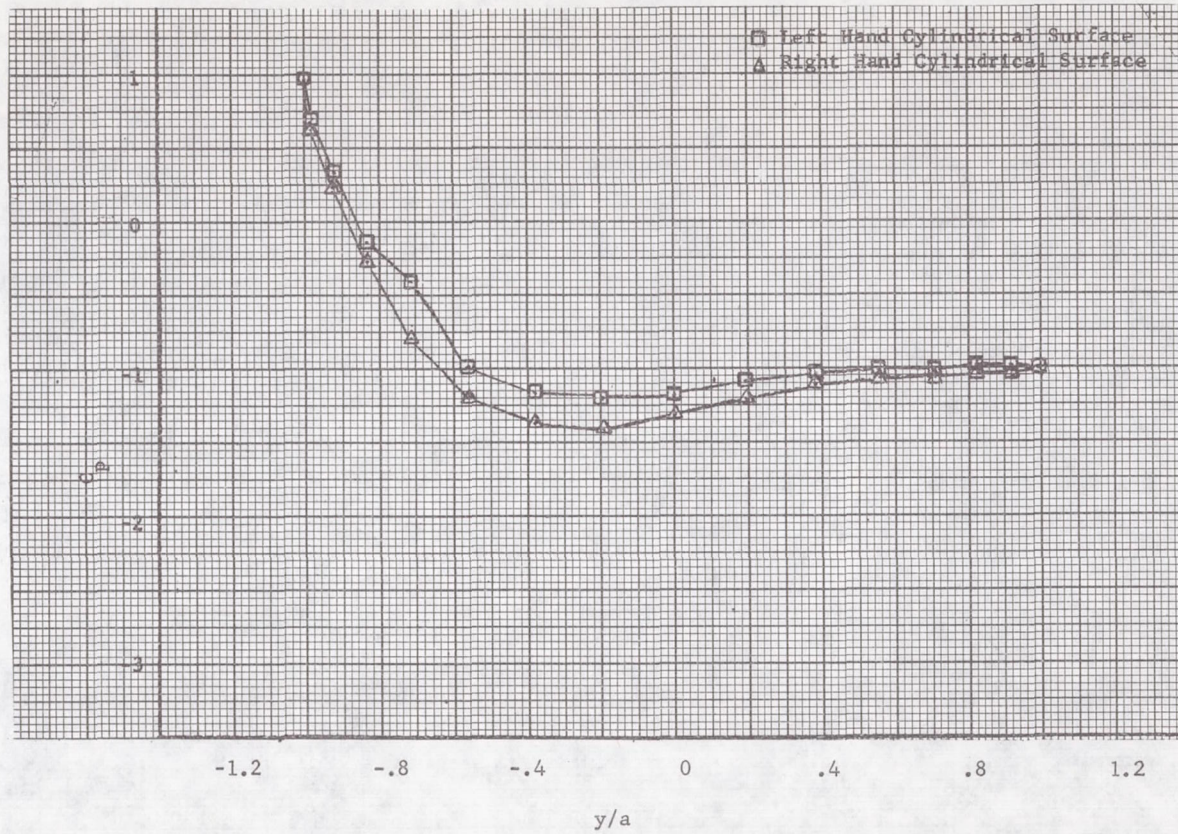


Figure 17
 Pressure coefficient distribution along the cylindrical surface at a time when the free stream particles have moved 10.45 cylinder diameters; Problem 133.0, Instantaneous Lift Coefficient, $C_L = 0.1665$.

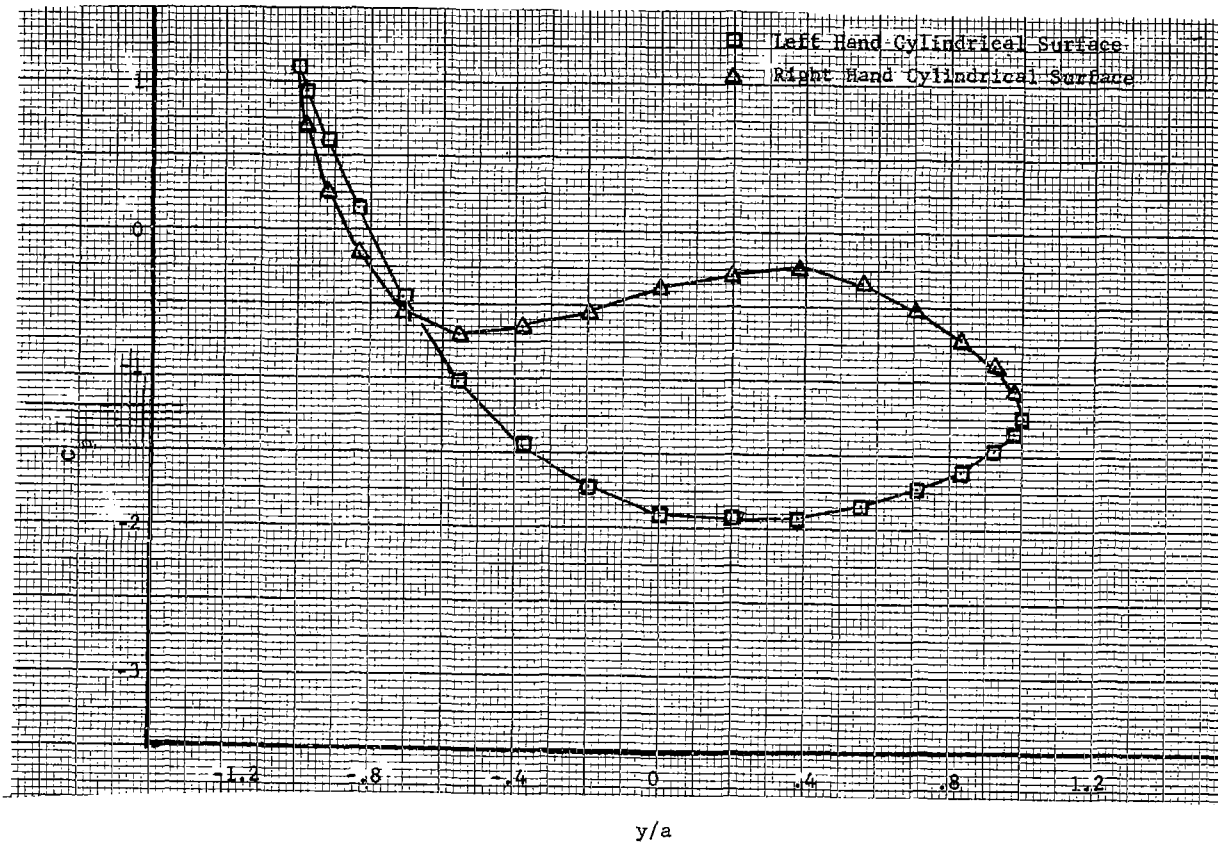
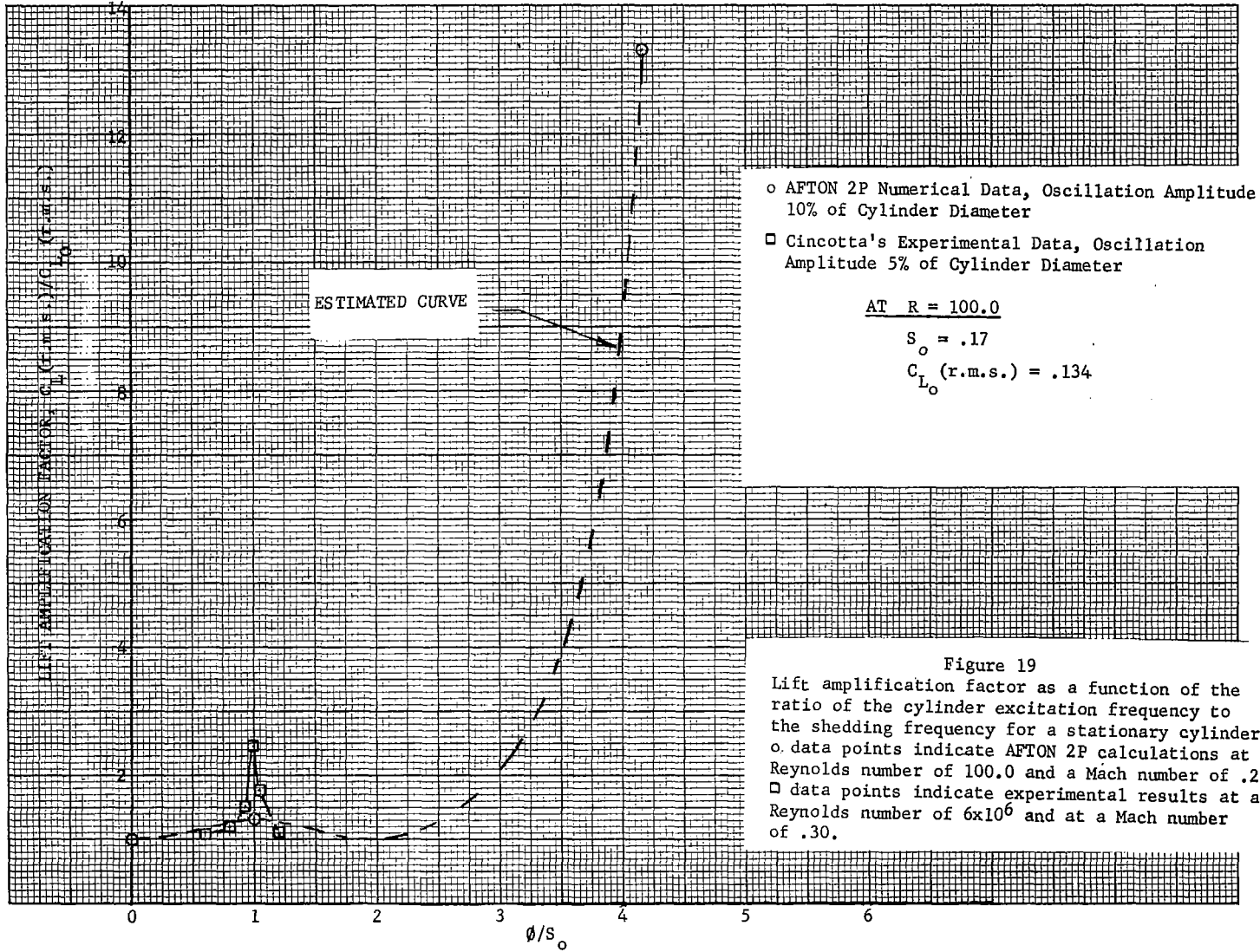


Figure 18
 Pressure coefficient distribution along the
 cylindrical surface at a time when the free
 stream particles have moved 10.65 cylinder
 diameters; Problem 133.2, Instantaneous Lift
 Coefficient, $C_L = -1.1$.



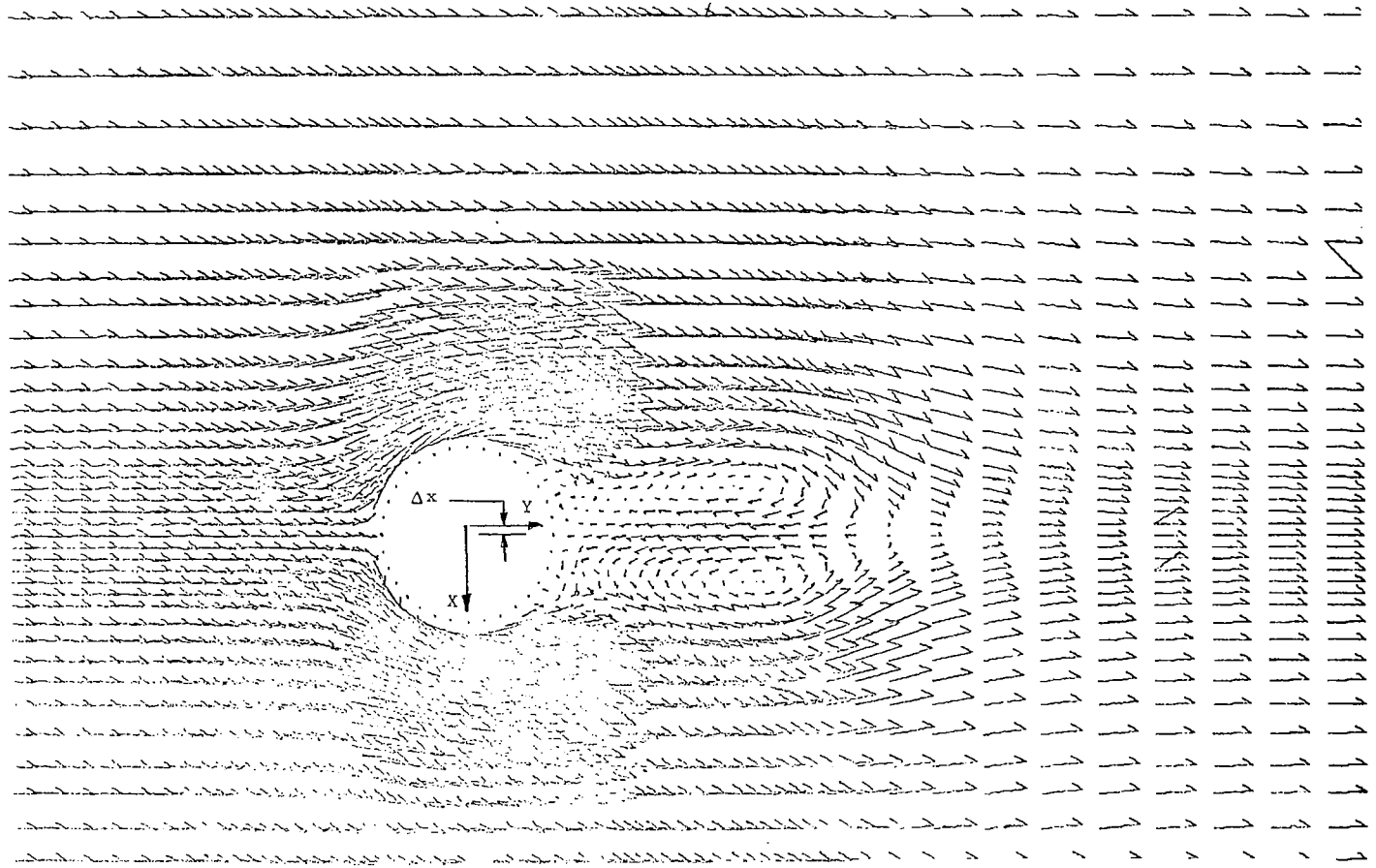


Figure 20

Velocity Vector Plot of the moving cylinder
 flow field at a time when the free stream
 particles have moved 5.08 cylinder diameters;
 Problem 133.1, $R = 1000.0$, $M_{\infty} = .20$; oscillation
 frequency 2.42 radians/msec, oscillation
 amplitude 10% of cylinder radius.

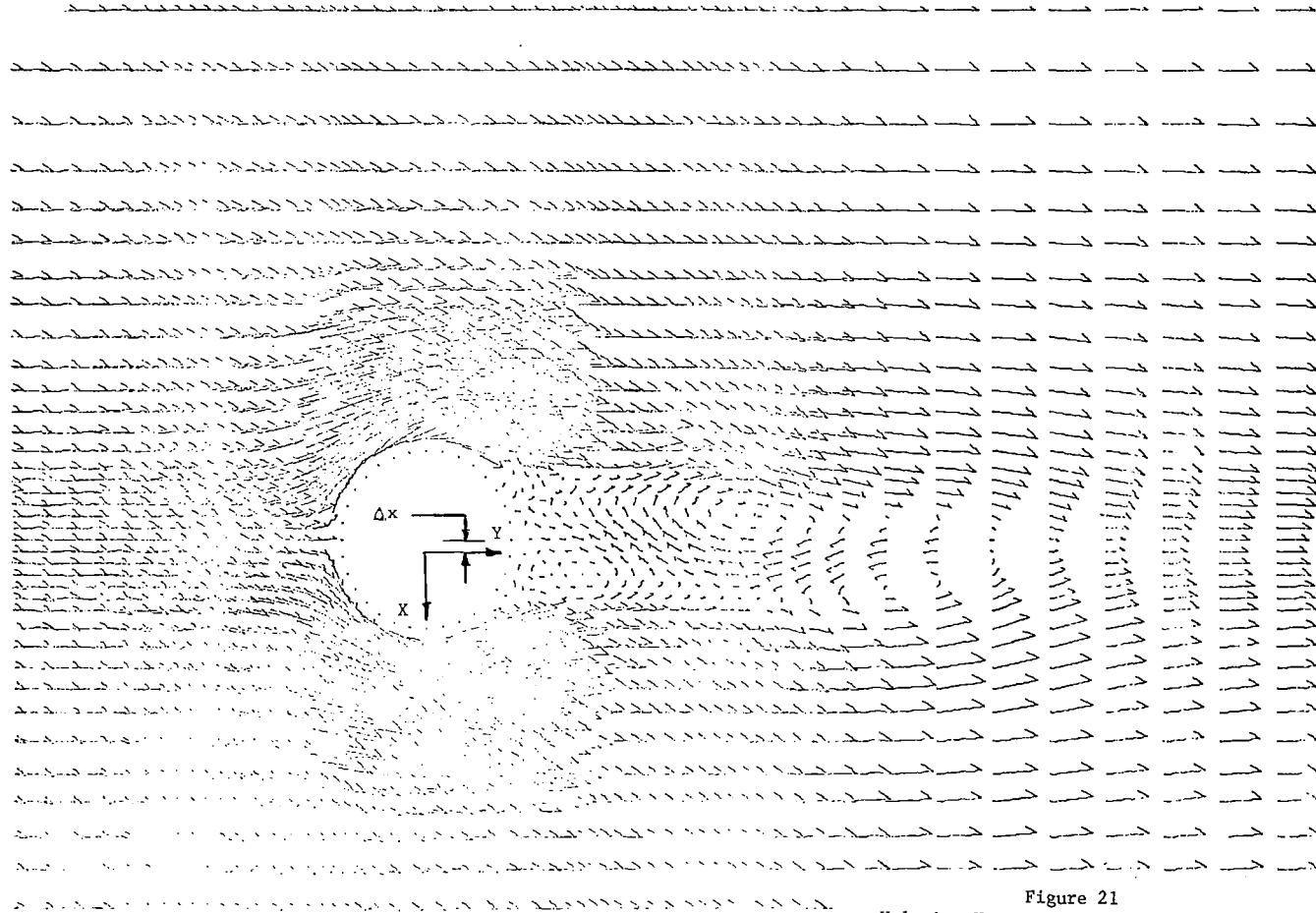


Figure 21

Velocity Vector Plot of the moving cylinder flow field at a time when the free stream particles have moved 7.625 cylinder diameters; Problem 133.1, $R = 1000.0$, $M_\infty = .20$; oscillation frequency 2.42 radians/msec, oscillation amplitude 10% of cylinder radius.

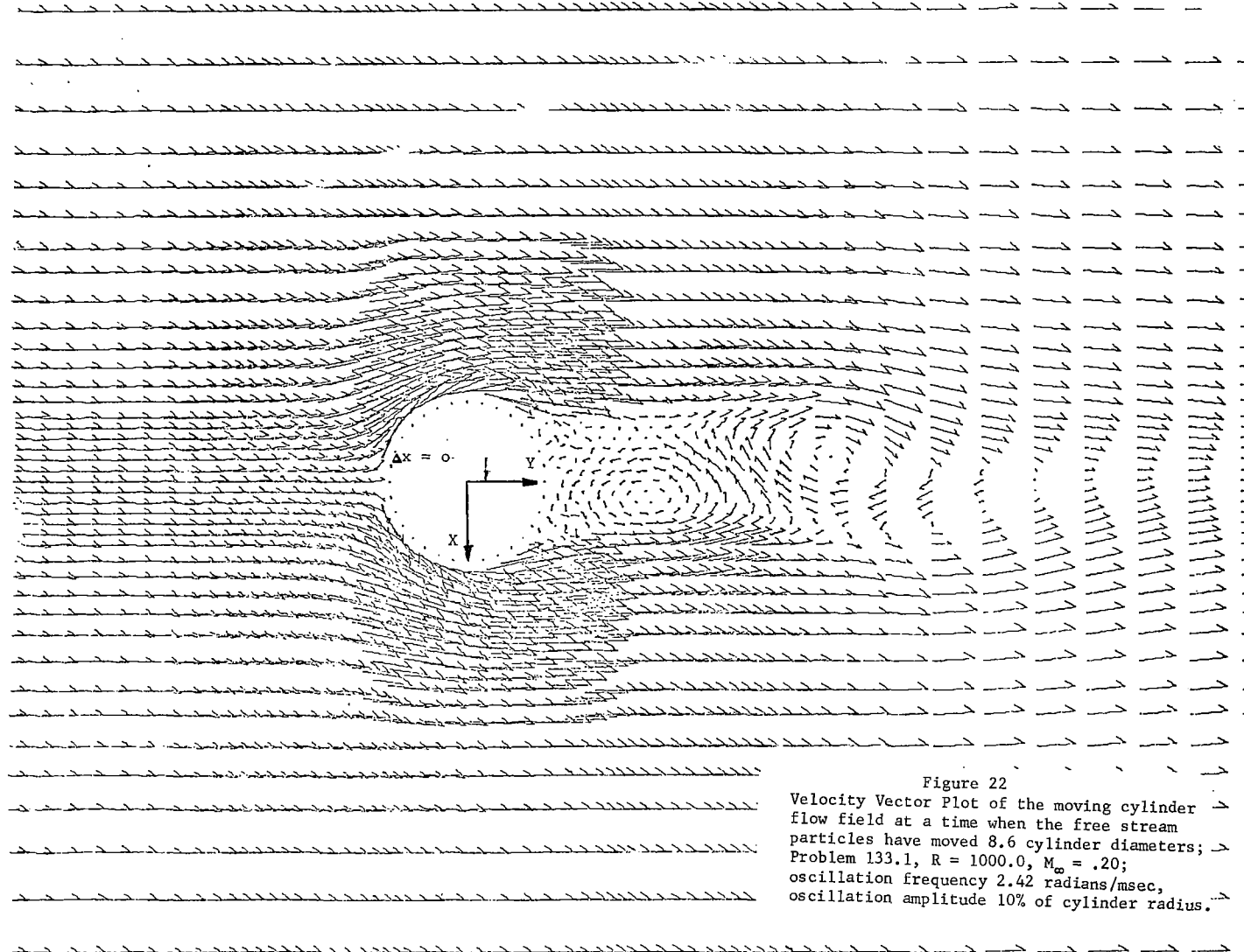


Figure 22
Velocity Vector Plot of the moving cylinder
flow field at a time when the free stream
particles have moved 8.6 cylinder diameters;
Problem 133.1, $R = 1000.0$, $M_\infty = .20$;
oscillation frequency 2.42 radians/msec,
oscillation amplitude 10% of cylinder radius.

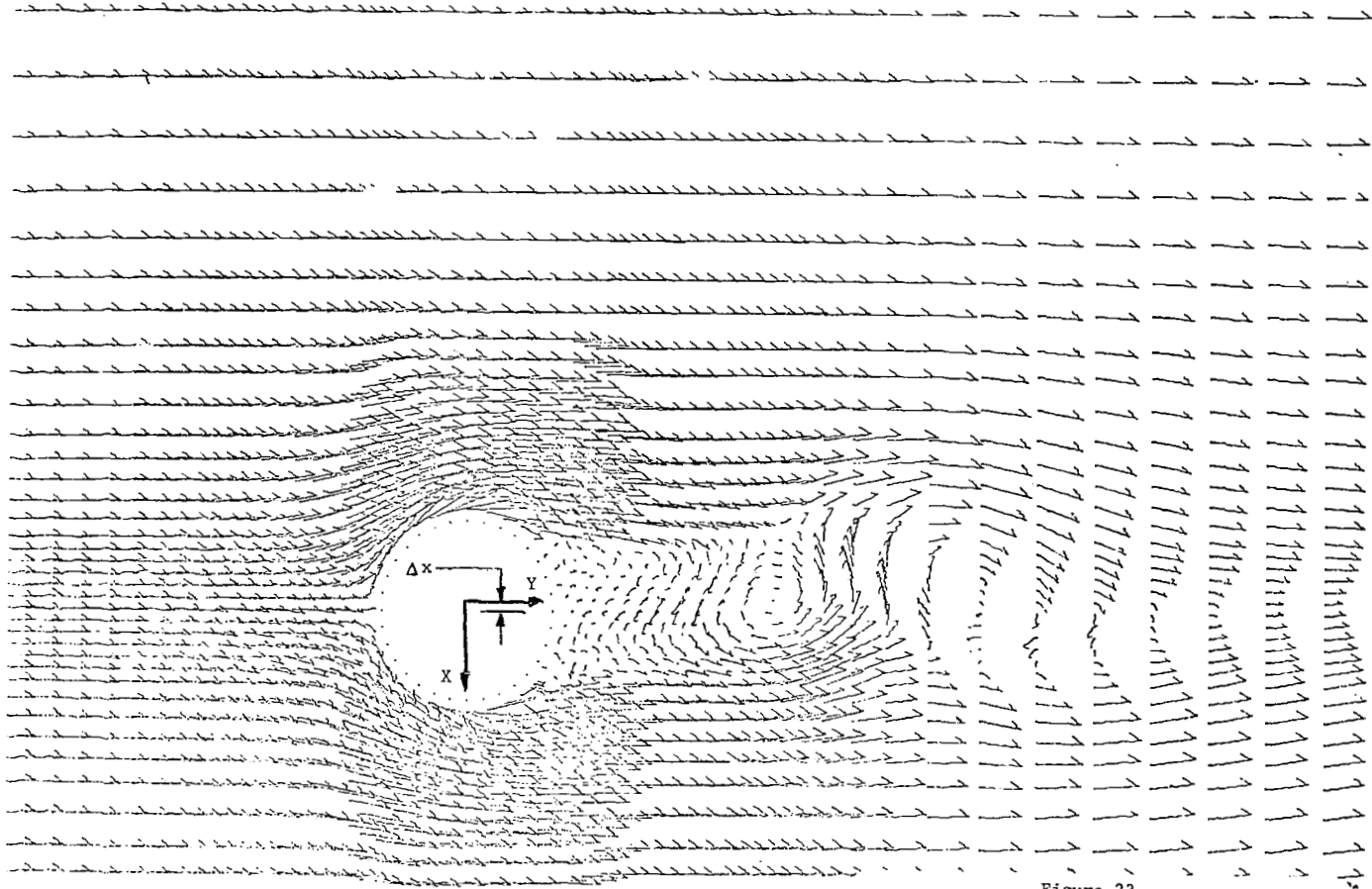


Figure 23

Velocity Vector Plot of the moving cylinder flow field at a time when the free stream particles have moved 9.68 cylinder diameters; Problem 133.1, $R = 1000.0$, $M_\infty = .20$; oscillation frequency 2.42 radians/msec, oscillation amplitude 10% of cylinder radius.

- o Measurements of Wieselsberger for $\phi = 0.0$
- Numerical Data for $\phi = 0.17$

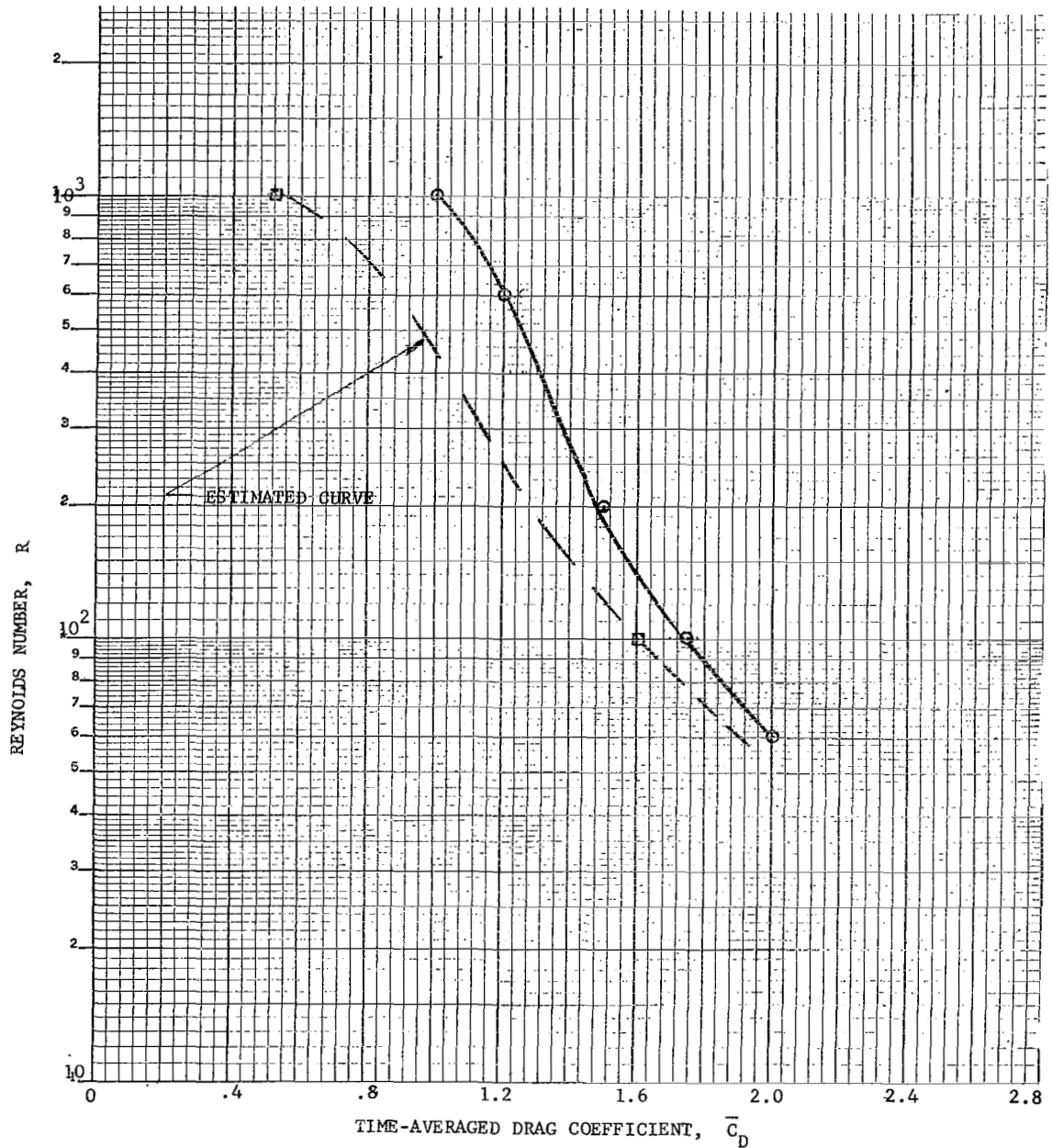


Figure 24
 Variation of time-averaged drag coefficient vs. Reynolds number; numerical data from Problems 133.1 and 133.0; experimental data of Wieselsberger,

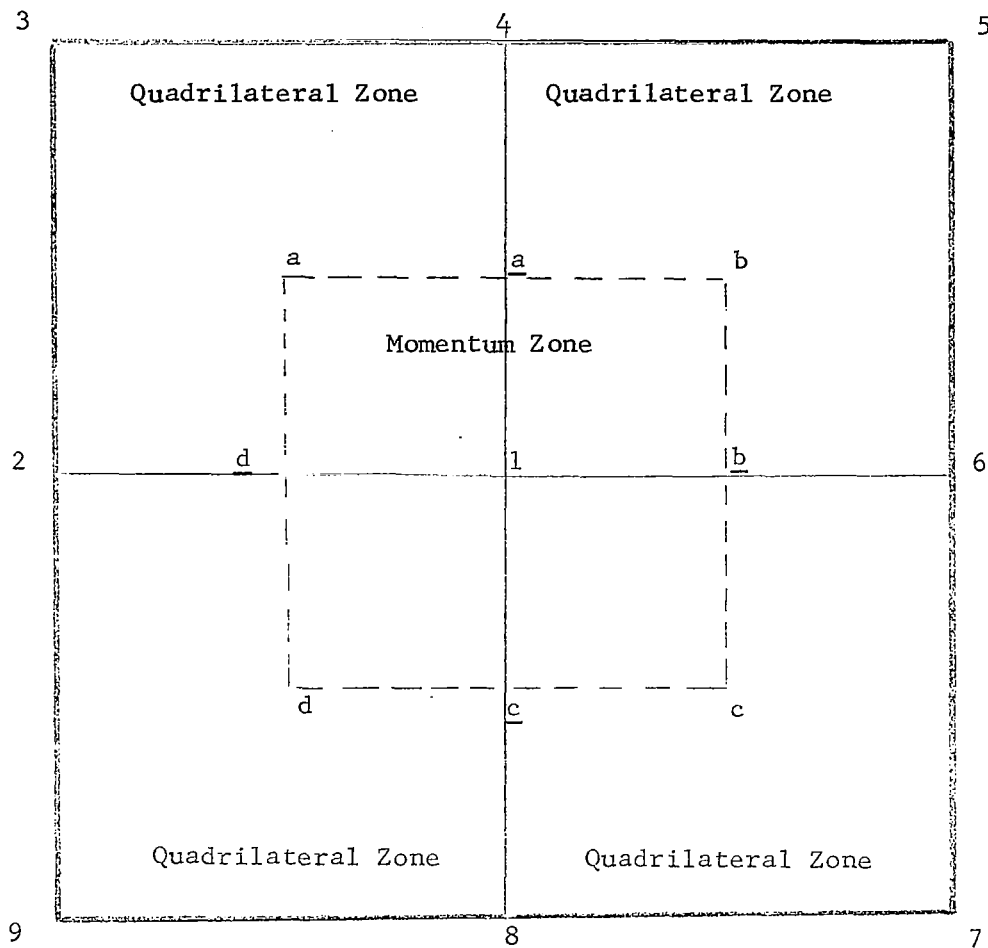


Figure 25

Schematic Diagram of an AFTON 2A or 2P Space Mesh, Showing a Momentum Zone and the Four Quadrilateral Zones Whose Corner Pieces Make Up the Momentum Zone.

4.0 REFERENCES

1. Cincotta, J. J., Jones, G. W., and Walker, R. W., "Aerodynamic Forces on a Stationary and Oscillating Circular Cylinder at High Reynolds Numbers," NASA TR R-300, 1969
2. Trulio, J. G., Niles, W. J., Carr, W. E., and Rentfrow, R. L., "Calculations of Two-Dimensional Turbulent Flow Fields," NASA, CR-430 (1966)
3. Trulio, J. G., and Walitt, L., "Numerical Calculation of Viscous Compressible Fluid Flow Around a Stationary Cylinder," Applied Theory Final Summary Report, Contract NAS 8-10034, April 1967 (to be published)
4. Trulio, J.G., "Theory and Structure of the AFTON Codes," Technical Report No. AFWL-TR-66-19 (1966)
5. Roshko, A., "On the Development of Turbulent Wakes from Vortex Streets," NASA Report 1191 (1954)
6. Schlichting, H., "Boundary Layer Theory, " McGraw-Hill (1960), p.16
7. Reference 6, p. 109
8. Reference 6, p. 75
9. Shih-I Pai, "Viscous Flow Theory," Volume I-Laminar Flow, Van Nostrand (1950), p. 300
10. Liepmann, H. W., and Roshko, A., "Elements of Gas Dynamics," Wiley (1957), p. 178